

Summer 8-2018

Development to a Flexible Surface Acoustic Wave Sensor for Strain Sensing

Neha Vedavathi Ramachandran
Embry-Riddle Aeronautical University

Follow this and additional works at: <https://commons.erau.edu/edt>



Part of the [Aerospace Engineering Commons](#)

Scholarly Commons Citation

Ramachandran, Neha Vedavathi, "Development to a Flexible Surface Acoustic Wave Sensor for Strain Sensing" (2018). *Doctoral Dissertations and Master's Theses*. 420.
<https://commons.erau.edu/edt/420>

This Thesis - Open Access is brought to you for free and open access by Scholarly Commons. It has been accepted for inclusion in Doctoral Dissertations and Master's Theses by an authorized administrator of Scholarly Commons. For more information, please contact commons@erau.edu.

DEVELOPMENT TO A FLEXIBLE SURFACE ACOUSTIC WAVE SENSOR FOR
STRAIN SENSING

A Thesis

Submitted to the Faculty

of

Embry-Riddle Aeronautical University

by

Neha Vedavathi Ramachandran

In Partial Fulfillment of the

Requirements for the Degree

of

Master of Science in Aerospace Engineering

August 2018

Embry-Riddle Aeronautical University

Daytona Beach, Florida


DEVELOPMENT TO A FLEXIBLE SURFACE ACOUSTIC WAVE SENSOR FOR
STRAIN SENSING

by

Neha Vedavathi Ramachandran

A Thesis prepared under the direction of the candidate's committee chairman, Dr. Daewon Kim, Department of Aerospace Engineering, and has been approved by the members of the thesis committee. It was submitted to the School of Graduate Studies and Research and was accepted in partial fulfillment of the requirements for the degree of Master of Science in Aerospace Engineering.

THESIS COMMITTEE



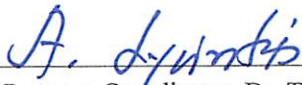
Chairman, Dr. Daewon Kim



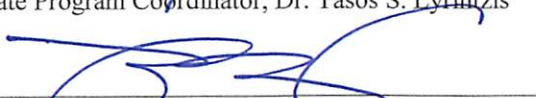
Member, Dr. Marwan Al-Haik



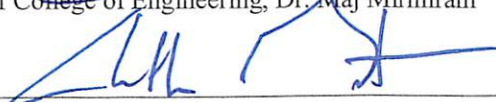
Member, Dr. Eduardo Rojas



Graduate Program Coordinator, Dr. Tasos S. Lyrintzis



Dean of College of Engineering, Dr. Maj Mirmirani



Vice Chancellor, Academic Support, Dr. Christopher Grant

9/14/18

Date

9/14/18

Date

9/14/18

Date

ACKNOWLEDGMENTS

I would like to express my deep gratitude to my advisor, Dr. Daewon Kim, for guiding and supporting me in every phase of this thesis work. His encouragement, no matter how well the research was proceeding, was always positive. He always corrected me when I was deviated and accelerated my work, wherever I was lagged. His patience, kindness and helping nature has always brought an inspiration in me on how welcoming a Professor could be.

This thesis wouldn't have been possible without proper guidance from Professor Rojas in showing me the right path to proceed at every stage. He was always available to discuss every issue that came by and it is an honor for me to thank him. On the other hand, Professor Al-Haik has always provided me a helping hand with the use of labs and access where I could use the fume hood to conduct the necessary experiments. I am obliged to him and I acknowledge him for his support and suggestions he provided, especially during the pre-defense that helped me work better in the direction that I otherwise would have deviated.

I would like to show my sincere gratitude to Mr. Mike Potash for helping me set up the experiment with the available devices and for carrying out the necessary electrical connections. He was always available at the office whenever I needed him. Also, I am very indebted to him for teaching me how circuits behave and for sharing his electrical knowledge. Mrs. Foram Madiyar has been one of my guides in a number of ways and I am really grateful to her. Being a chemistry Professor, she has not only helped me mix the chemicals proportionately, but she was the one who brought about

the confidence within me that this research could be accomplished even though it had many procedures that an Aerospace engineer haven't used before.

My deepest gratitude goes to Professor David Sypeck for providing me access to the Materials lab, where I completed my report, modelling, and analysis tasks. Being one of the tidiest and hardworking Professors in the AE department, he has never hesitated to provide me access to any equipment's that I asked for that helped me conduct my experiments.

My heartfelt of thanks goes to my parents and brother, who have always embraced my decisions and encouraged my work. Last but not the least, I am indebted to all my friends especially Srikar Kuthuru, Vijay Sai, Cannelle, Vivek Chandru Padmanaban, Ademola and Finian who provided me the necessary support in completing this thesis.

Thank you all.

TABLE OF CONTENTS

ACKNOWLEDGMENTS.....	i
LIST OF TABLES.....	v
LIST OF FIGURES	vi
SYMBOLS.....	viii
ABBREVIATIONS	ix
NOMENCLATURE	x
ABSTRACT.....	xi
1. Introduction.....	1
1.1. Acoustic Wave Sensor	1
1.1.1. Classification of Acoustic Wave Sensors	2
1.2. Surface Acoustic Wave (SAW) Devices	5
1.3. Piezoelectricity.....	7
1.4. Piezoelectric Materials	9
1.5. Phases of PVDF.....	13
1.6. Interdigital Transducer (IDT)	16
1.7. Objectives and Approaches	18
2. SAW Device Modelling	20
2.1. Working Principle	20
2.2. Design Parameters	21
2.3. Impulse Response Model.....	23
2.4. Coupling of Modes (COM) Theory	25
2.5. Equivalent Circuit Model.....	26
2.6. Transmission Matrix Approach.....	28
3. Fabrication and Testing	32
3.1. Fabrication	32
3.1.1. Preparation of Composite Substrate	32
3.1.2. Poling of the Composite.....	39
3.1.3. Fabrication of IDT	42
3.2. Testing:.....	47
3.2.1. Testing of the 0-3 Composite	47
3.2.2. Piezoelectric Testing of the Composite Substrate	53
3.2.3. Testing of the SAW Device.....	54
4. Results and Discussions.....	55
4.1. Results in Substrate Fabrication	55
4.1.1. Light Microscopic Image	55
4.1.2. Scanning Electron Microscopic (SEM) Image.....	55
4.1.3. Comparative Study of PVDF-TrFE/PZT and PVDF/PZT Composites:	57

4.2.	Photomask Design and Development	58
4.3.	SAW Responses Using MATLAB	62
4.4.	Testing of the SAW Device	64
5.	Conclusion	70
6.	Future Work	73
7.	Recommendation	74
8.	References.....	75
9.	Appendix.....	82
A.	IDT calculations for mathematical calculations	82
B.	MATLAB Simulation for First Order Response	84
C.	MATLAB Simulation for Second Order Response	87

LIST OF TABLES

Table 1: Electromechanical and dielectric properties of PVDF and PZT.....	11
Table 2: Mechanical and piezoelectric properties of PVDF and PZT-5H.....	12
Table 3: Chemical composition of the composite.....	56
Table 4: SAW device parameters.....	58
Table 5: Modified IDT dimensions.....	59

LIST OF FIGURES

Figure 1. Electromechanical sensors classification.....	1
Figure 2. Types of piezoelectric sensing.....	2
Figure 3. Classification of acoustic wave sensor.	3
Figure 4. SAW delay line sensor.	6
Figure 5. Polarization process.....	7
Figure 6. Direct and inverse piezoelectric mechanisms.....	8
Figure 7. PZT, PVDF and PVDF-TrFE powder.	10
Figure 8. 0-3 Particle distribution in a composite.....	11
Figure 9. α , β and γ phases of PVDF.	14
Figure 10. Methods to achieve β phase of PVDF.	15
Figure 11. IDT configurations.	16
Figure 12. Top and side view of SAW device.....	17
Figure 13. Interrogation of several SAW sensors simultaneously.....	20
Figure 14. Wave generated by IDT fingers excitation.....	21
Figure 15. 3-Port representation of an IDT.....	25
Figure 16. Side-view of interdigital transducer	26
Figure 17. Masons equivalent circuit for one finger of an IDT in cross-field approximation.	27
Figure 18. Block structure of SAW delay line sensor.....	28
Figure 19. Schematics of a single finger of IDT in side-view.	29
Figure 20. a) Weighing PVDF using a digital balance, b) Measured PVDF powder.....	34
Figure 21. a) Measuring DMSO, b) Heating the PVDF-DMSO mixture.....	35
Figure 22. a) and b) PVDF-PZT-DMSO mixture subjected to ultrasound.....	36
Figure 23. a) Oven heating of the solution to evaporate DMSO b) Hot-pressing the dried mass.....	36
Figure 24. PVDF/PZT sample cooled to room temperature and let dry for a day to get the flat round composite.	37
Figure 25. a) PVDF/PZT 0-3 Composite after it is cut.....	38
Figure 26. Flexible sensor substrate.....	38
Figure 27. Shows the gold sputtered samples.	40
Figure 28. Immersed substrate in Si oil bath for polarization.....	41
Figure 29. Polarization of PVDF/PZT composite.....	42

Figure 30. Spin coating of the sample.....	44
Figure 31. Sample coated with photoresist.	44
Figure 32. Sample coated with photoresist placed against photomask prepared to be UV exposed.	45
Figure 33. Photoresist coated sample exposed to UV radiation.	46
Figure 34. a) Developing the UV radiated sample b) Etching the unexposed gold.....	47
Figure 35. Graph comparing the IR absorbance of PVDF, PVDF-TrFE, and PZT.....	49
Figure 36. FTIR absorbance plot for PVDF/PZT 0-3 composite.	51
Figure 37. XRD plot representing the chemical composition in the obtained composite.	52
Figure 38. d33 measurement of the polarized sample.	53
Figure 39. Device used to set mN force to the sample.	54
Figure 40. Microscopic image of the substrate a) Top-view, b) Bottom-view.....	55
Figure 41. SEM images with a) Non-uniform particle distribution in PVDF matrix	56
Figure 42. SEM images used for comparison of volume fraction.	57
Figure 43. IDT design sketched on Layout Editor.....	59
Figure 44. Modified IDT design sketched on Layout Editor.....	60
Figure 45. Modified IDT design sketched on Layout Editor.....	61
Figure 46. a) IDTs developed using photolithographic process, b) IDT fingers visualized under a microscope.	62
Figure 47. Shows the frequency response, insertion loss, admittance, conductance, and susceptance obtained from the first order impulse response model.	63
Figure 48. Represents the frequency response of the second order cross-field model. ...	64
Figure 49. a) and b) Sensor attached to Network Analyzer through the RF probes.	65
Figure 50. SAW transmission signal displayed on Network Analyzer.....	66
Figure 51. SAW transmission curve.	66
Figure 52. SAW phase curve.	68

SYMBOLS

S_{ij}	=	Strain component (m/m)
s_{ijkl}	=	Elastic compliance constant (m^2/N)
T_{kl}	=	Stress component (N/m^2)
d_{kij}	=	Piezoelectric constant (C/m)
D_i	=	Electric displacement component (C/m^2)
ε_{ik}	=	Permittivity component (F/m)
E_k	=	Electric field component (V/m)
f_o	=	resonant frequency
v	=	acoustic velocity
λ	=	acoustic wavelength
α, β	=	Phases of PVDF
$\gamma, \delta, \varepsilon$	=	Phases of PVDF
B	=	fractional bandwidth
N_p	=	number of finger pairs needed
Z	=	impedance of IDT
C_t	=	total capacitance of the sensor
C_o	=	capacitance per finger pair per unit length
W	=	aperture or overlap between fingers
$\varphi(f)$	=	magnitude of frequency response
G_a	=	Radiation conductance
B_a	=	Acoustic susceptance
E	=	Electric Field
T	=	Permittivity Component
K	=	Coupling coefficient
Y	=	Admittance
R_g	=	Load resistance
Z	=	Impedance
V	=	Voltage
θ	=	Phase Angle
ϵ	=	Material permittivity

ABBREVIATIONS

SAW	Surface Acoustic Wave
IDT	Inter Digital Transducer
NBW	Null Bandwidth
BAW	Bulk Acoustic Wave
SH-APM	Shear-horizontal acoustic plate mode
FPW	Flexural-plate wave
SH-SAW	Shear-horizontal surface acoustic wave
SSBW	Surface-skimming bulk wave
TSM	Thickness shear mode
STW	Surface transverse wave
STW	Surface transverse wave
FTIR	Fourier-transform Infrared Spectroscopy
MEMS	Micro-Electromechanical System
RF	Radio Frequency
LW	Low Wave
QCM	Quartz Crystal Microbalance
RFID	Radio Frequency Identification
COM	Coupling of Modes
FFT	Fast Fourier Transform
IL	Insertion Loss
CVD	Chemical Vapor Deposition
PVD	Physical Vapor Deposition
UV	Ultra Violet
IR	Infra Red
XRD	X-Ray Diffraction
SEM	Scanning Electron Microscope
MHz	MegaHertz
FEM	Finite Elemental Analysis

NOMENCLATURE

PVDF	Polyvinylidene fluoride
PZT	Lead zirconate titanate
DMF	N, N-Dimethylformamide
DMSO	N, N-Dimethyl sulfoxide
SiO ₂	Quartz
LiNbO ₃	Lithium niobate
LiTaO ₃	Lithium Tantalate
BaTiO ₃	Barium Titanate
PbTiO ₃	Lead Titanate
Pb(Zr _x Ti _{1-x})O ₃	Lead Zirconium Titanate
PZ	Lead Zirconate
PT	Lead Titanate
EAP	Electro-Active Polymers
PI	Polyimide
CH ₂ -CF ₂ -	Repeating Monomer
PZT – 5H	Navy Type VI PZT
Al ₂ O ₃	Aluminum Oxide
NMP	N-methyl-2-pyrrolidone
DMAc	Dimethylacetamide
Al foil	Aluminum foil

ABSTRACT

Vedavathi Ramachandran, Neha, MSAE, Embry-Riddle Aeronautical University, Aug 2018. Development to a flexible surface acoustic wave sensor for strain sensing.

Surface acoustic wave (SAW) sensors have increasing demand in structural health monitoring due to its passive, variable bandwidth, reliable life-cycle, high accuracy, small size, and light nature. SAW sensors can not only provide the static states of the structural system, such as temperature and pressure but also enable continuous real-time monitoring of dynamic states including strains. SAW sensors are generally fabricated with a rigid piezoceramic substrate, incapable of adapting to highly curved surfaces or flexible objects. The ongoing demands of sensor adaptability with flexible substrates, which is also capable of wireless monitoring, is the basis of the research that can be applied to medical and aerospace fields.

The SAW fabrication involves developing a composite substrate using hot-pressing and depositing the interdigital transducers using additive manufacturing. The substrate of the SAW sensor is fabricated by integrating lead zirconate titanate (PZT) ceramic nanoparticles as a reinforcement into polyvinylidene fluoride (PVDF) polymer matrix in the 0-3 direction. This enables the substrate to attain enhanced piezoelectric properties along with improved mechanical strength. PVDF is dissolved in a strong polar solvent such as N, N- dimethyl sulfoxide to which 50 wt. % of PZT powder is added to impart optimum dielectric property maintaining flexibility. Stretching by hot-pressing this mixture above the melting point of PVDF enables the transformation of non-polar α to a polar β crystalline phase of PVDF. The amount of

β crystalline phase of the substrate produced out of stretching the PVDF is observed under FTIR scanning.

Research has also been conducted by using a PVDF-TrFE, a copolymer of PVDF and brief comparison study on the flexibility of the composite developed using PZT/PVDF and PZT/PVDF-TrFE is performed.

Polarization is conducted by sputtering gold on both sides of the thin substrate and subjecting it to a high electric field in a silicone oil bath to prevent arcing. The dielectric properties of the sample are measured by which frequency and attenuation are calculated mathematically. Delay-line IDTs are attached to it using conventional photolithography technique. With the sensor being developed, radio frequency signal is passed through an interrogator to the antenna connected to the input transducer which transfers the signal in the form of Rayleigh waves. The frequency response of the SAW device changes in amplitude and phase when subjected to temperature, pressure, or strain changes. FEM model of the SAW sensor is conducted, and the resulting deformation simulation is performed. This thesis discusses the development process of a flexible piezocomposite SAW sensor.

1. Introduction

1.1. Acoustic Wave Sensor

A sensor is a device that responds to a stimulus such as light, pressure or thermal changes and can generate signals that can later be measured or interpreted. Based on the types of sensors used for object detection, a sensor can be divided into 7 sub-divisions namely electro-mechanical, pneumatic, magnetic, inductive, capacitive, photoelectric and ultrasonic [1]. Each of these divisions also has subcategories, such as shown in Figure 1 for electromechanical sensors.

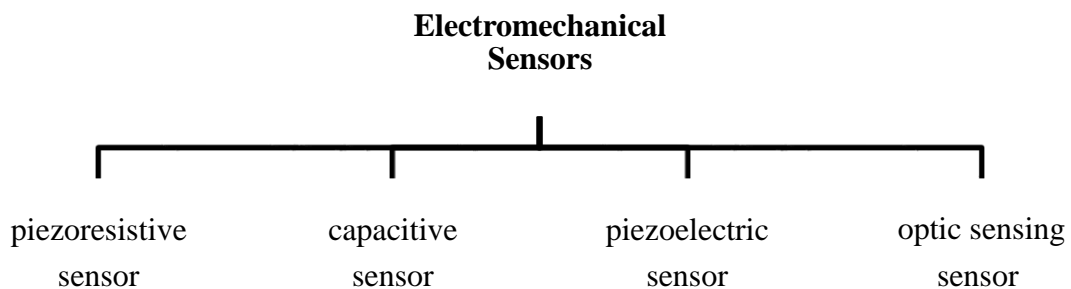


Figure 1. Electromechanical sensors classification.

Acoustic wave sensor, which is a part of the piezoelectric sensor, is a sub-branch of microelectromechanical system (MEMS) shown in Figure 2 capable of sensing physical phenomenon over a body by means of acoustic wave propagation. These are small lightweight devices which generally use the piezoelectric material for acoustic wave generation and propagation. They are made passive and wireless and provide simultaneous multi-sensor interrogation with a range of few centimeters to several 100s of a meter.

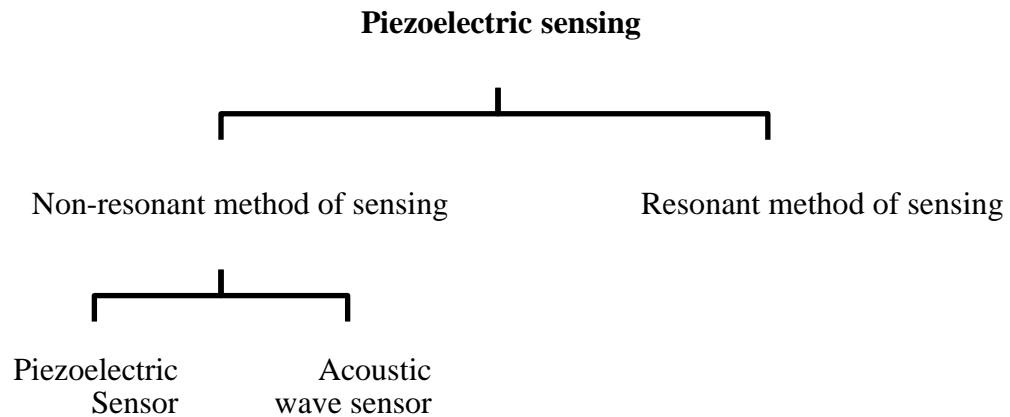


Figure 2. Types of piezoelectric sensing.

1.1.1. Classification of Acoustic Wave Sensors

Acoustic wave sensors are classified as Surface Acoustic Wave (SAW) [2] sensors and Bulk Acoustic Wave (BAW) sensors based on the direction of wave propagation. BAW sensors generate waves that propagate through the body of the substrate, whereas, SAW sensors generate waves that propagate on the surface of the substrate. These are further classified as shown in Figure 3. The mode of propagation of these waves enables the sensors to possess varied responsibilities and could be used in different conditions.

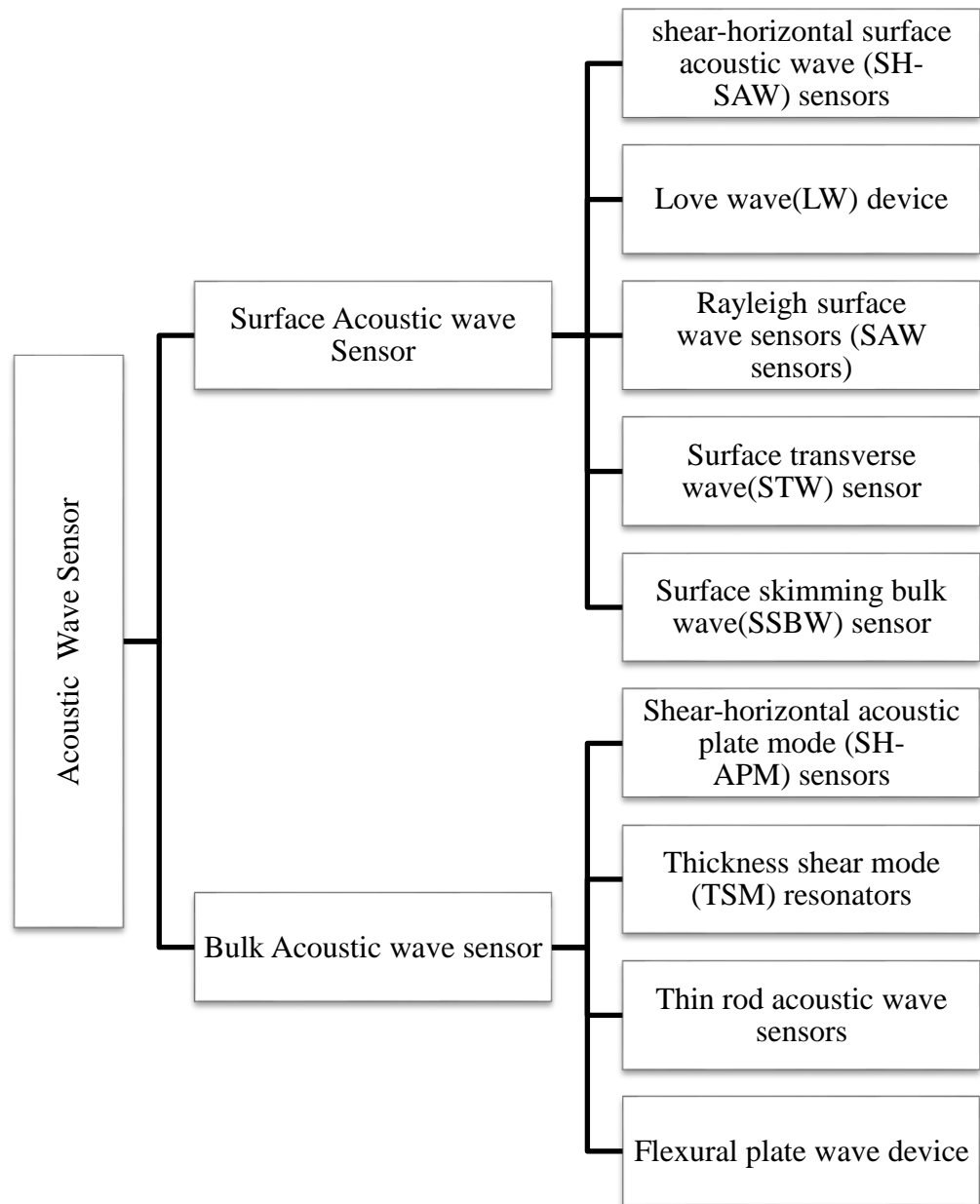


Figure 3. Classification of acoustic wave sensor.

In case of Shear-Horizontal Surface Acoustic Wave (SH-SAW) sensors, the particles are displaced in a shear-horizontal direction only and are partially confined to the

surface penetrating to several wavelength depths. These devices can be operated in a liquid medium. This is different from the SAW-based Rayleigh wave sensor where the particles displace both in the horizontal and transverse directions to its motion resulting in an elliptical displacement of particles in the substrate material. The two-dimensional Rayleigh waveform is confined to a surface depth of one wavelength. These devices cannot be operated in the liquid medium due to their dissipation of motion in the transverse direction.

Love wave-based SAW device has a lower acoustic velocity in the layered surface than the piezoelectric substrate and is polarized only in the shear horizontal direction. Due to the accumulation of acoustic waves in the thin guiding layer, these sensors exhibit high sensitivity. Recent studies have led to the discovery of surface skimming bulk waves (SSBW) and leaky wave, which both are the SH-SAWs [2]. SSBWs propagates just beneath the surface of the substrate. On the other hand, plate wave or Lamb wave propagates in the region between the two layers of a thin plate of extremely less thickness compared to the acoustic wavelength. The Flexural plate is the lowest anti-symmetric mode of Lamb waves.

SH-APM are shear-horizontal waves that are polarized in a direction parallel to the acoustic plate surface. These waves propagate as the waves reflect in the region between the two layers of the plate and hence the Shear-horizontal displacement occurs on both the metalized surface and the free surface.

Thickness shear mode (TSM) resonators or the quartz crystal microbalance (QCM) [3] were initially seen to produce shear deformation in a thin disk of AT-cut quartz when a voltage was applied between two electrodes placed on each side.

In case of the thin rod acoustic wave sensor, thin rod of a circular cross-section of diameter much smaller than the acoustic wavelength produce flexural and longitudinal waves as the piezoelectric transducers integrated on them generates and receives wave signals.

1.2. Surface Acoustic Wave (SAW) Devices

SAW sensors were first discovered by Lord Rayleigh in 1851 [4]. It was only in 1965 that these sensors came into the practical application when R. M. White and F. W. Voltmer invented the interdigital transducer (IDT) which were capable of exciting acoustic waves and detecting defects when mounted on the SAW substrate [5]. Since then these sensors have found to have diverse applications in telecommunications and signal processing.

The term interdigital refers to digit-like or finger-like periodic patterns. The discovery of IDT has given a huge rise in the development of electronic filters, convolves, delay lines, resonators, oscillators, pulse compression filters for radar, and many more [6, 7]. In around 1980s, due to the advance in mobile radio that required filters, the need for these devices dramatically raised. Telecommunication industry has seen the highest increase in the usage of such devices with around 3 billion filters being developed annually.

SAW devices have been used to measure physical quantities such as temperature, pressure, strain, stress, and humidity [8, 9]. Presently, they are being employed in moving or rotating parts including automotive drive train systems and power steering applications capable of being monitored from a distance.

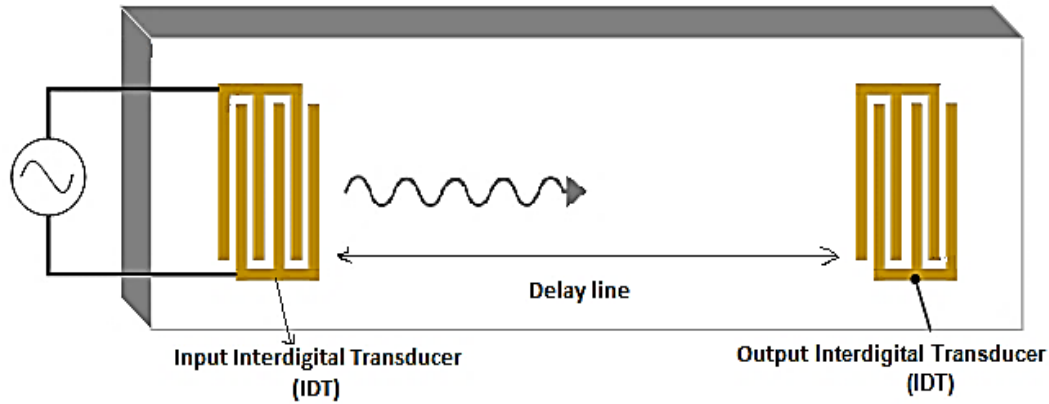


Figure 4. SAW delay line sensor.

SAW delay line sensors are highly attractive due to their many desirable features such as high performance, easy fabrication, and good reproducibility. Figure 4 shows a typical delay line SAW sensor consisting of transmitter (input) IDT, receiver (output) IDT, and a delay line region. The delay line region is the surface where the acoustic wave in the form of Rayleigh waves propagates from the input to the output IDT. SAW sensors have many advantages compared to other sensors. However, conventional SAW sensors cannot be operated in hazardous environments such as in high-temperature, high-voltage plants, and high-vacuum process chambers, therefore, passive wireless sensors are developed in recent years for all contactless measurements [10-13]. Apart from its use in many domestic and industrial applications, wireless SAW sensors are also used in the medical field for measuring blood pressure [14].

Despite its many advantages and applications, SAW sensors are also not flexible which limits its applications to simple planar surfaces. The main objective of this research project is to create a passive wireless SAW sensor using a flexible substrate for strain sensing in complex surface systems. The work presented in this research gives a brief literature review of SAW sensor, their advantages, and disadvantages, design parameters required for SAW device

modelling, IDT modelling and losses associated with it, fabrication of the flexible piezoelectric substrate and the delay-line IDTs, and finally concludes with the mathematical modelling, results, and conclusion.

1.3. Piezoelectricity

SAW devices are operated based on piezoelectric effect. The piezoelectric effect is the material's ability to generate an electric charge when mechanical stress is applied. This effect is also reversible, i.e., imparting electric field produces stress. This effect was first discovered by French physicists Jacques and Pierre Curie in 1880. Piezoelectric materials have anisotropic dielectric responses making it capable of converting between mechanical and electrical energy. One of the main properties of dielectrics is that they do not possess free electrical charges or dipoles until an external electric field is applied and polarization occurs due to the interaction between the electric field and the structure. Ferroelectricity is a phenomenon under piezoelectricity where the materials remain polarized even after the electrical field is removed. Figure 5 shows the unpolarized and polarized structure of a piezoelectric material.

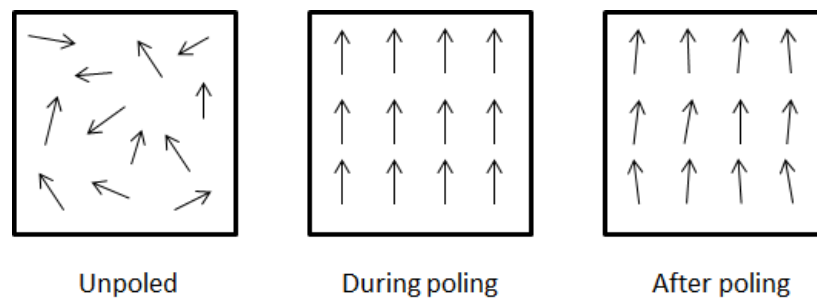


Figure 5. Polarization process [15].

As mentioned, the piezoelectric effect is the linear electromechanical interaction between the mechanical and electrical state of the material, so piezoelectric materials are

mainly divided into sensors and actuators based on the type of effect, i.e., direct or inverse piezoelectric effect. Direct piezoelectric effect converts the applied mechanical stress into measurable electrical charge, and inverse effect converts the applied electrical signals into displacement or force. Figure 6 shows the mechanisms of both direct and inverse piezoelectric effects. In case of direct effect, when the disc compresses the generated voltage has the same polarity as a poling voltage and when the disk expands the polarity is opposite. In the inverse effect, the disk enlarges when the applied voltage has the same polarity as poling voltage and compresses when it is opposite.

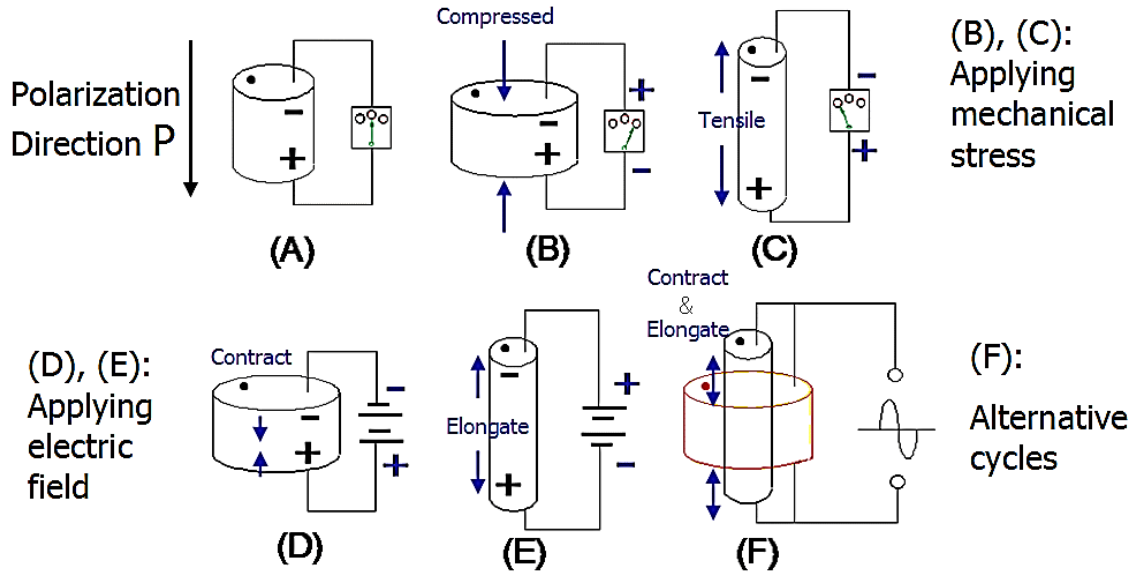


Figure 6. Direct and inverse piezoelectric mechanisms [16].

SAW input IDT performs the work under inverse piezoelectric effect where the applied electric field actuates the piezoelectric material and SAW output IDT acts as a sensor which detects the acoustic waves generated on the piezoelectric material and converts it back into electrical signals. The basic piezoelectric equations for the measurement of strain or displacement in the material are derived from Gibbs free energy equations given by:

$$S_{ij} = s_{ijkl}^E \sigma_{kl} + d_{kij} E_k \quad (1)$$

$$D_i = d_{ikl}^T \sigma_{kl} + \varepsilon_{ik}^\sigma E_k \quad (2)$$

Equation 1 [17] describes the inverse piezoelectric effect, where S is the strain component and E indicates the compliance constant, s^E indicates that the measurement was performed at zero electric fields, i.e., $E=0$. Similarly, Equation 2 describes the direct effect where D is the electric displacement component, and T indicates the permittivity component, σ indicates the stress, ε^σ indicates that no applied stress when the electric displacement is measured, i.e., $\sigma=0$. The indices i, j, k indices describe the three-dimensional space in bulk.

1.4. Piezoelectric Materials

Piezoelectric substrates are usually made of piezoelectric ceramics, and the largest structure type of piezoelectric ceramics belongs to perovskite family which consists of mixed oxides with O^{2-} ions at the corners of an octahedral structure [18]. Few of the piezoelectric ceramics used for generating the substrate of SAW sensor include single crystal materials: quartz (SiO_2), lithium niobate ($LiNbO_3$) and lithium tantalate ($LiTaO_3$), barium titanate ($BaTiO_3$), lead titanate ($PbTiO_3$) and lead zirconate titanate ($Pb(Zr_xTi_{1-x})O_3$ or PZT) [19].

The most commonly used ceramic is PZT, a binary solution of lead zirconate (PZ, an antiferroelectric) and lead titanate (PT, a ferroelectric) which finds its use in many applications due to its many desirable properties including high elastic modulus, high electromechanical coupling factor, and excellent frequency-temperature characteristics. However, PZT and other ceramic substrates are brittle and have a low tensile strength which limits their application. Therefore, piezoelectric polymers are used instead of ceramics making the sensors more flexible. Use of polymers as a substrate is not a new concept. In fact, a significant amount of work is carried out in electronics such as e-paper displays, microprocessors, and radio

frequency identification (RFID) tags [20]. Figure 7 shows the PZT, PVDF and PVDF-TrFE powders used for fabrication.



Figure 7. PZT, PVDF and PVDF-TrFE powder.

The use of flexible SAW sensors for structural health monitoring has been investigated in the recent years and comparison between piezoelectric crystals/ceramics such as Quartz and LiNbO₃ and electroactive polymers (EAP), such as polyimide (PI) and Polyvinylidene Fluoride (PVDF) are studied. Devices with polymer base have a quicker response time and very low density when compared to piezoelectric ceramics and are suitable for both actuation and sensing mechanisms. Among the EAPs, PVDF has become appealing to many industries due to its striking characteristics [21]. PVDF consists of long chains of the repeating monomer (-CH₂-CF₂-). They are inexpensive, lightweight, biologically compatible, mechanically stable structures and have high electromechanical coefficients which make them suitable as a piezoelectric substrate. They can undertake a significant amount of deformation while maintaining sufficient forces. PVDF also has a low electroactive response, and PVDF

actuators require high voltage power which limits their applications. Table 1 shows the electromechanical and dielectric properties of PZT and PVDF [22-23].

Table 1: Electromechanical and dielectric properties of PVDF and PZT.

Material	d_{33} ($\times 10^{-12}$ C/N)	ϵ_{33}/ϵ_0	k (%)
PVDF	-33	6-12	20
PZT 5-H	~ 580	~ 3500	65

From Table 1, the electromechanical properties of PZT 5-H are significantly higher than PVDF. PVDF has a dielectric constant K_{33} in the range of 6-12 whereas PZT has the constant at approximately 3500, also the coupling coefficient (k) of PVDF is at 0.2 and PZT is at 0.65. Apart from the low electromechanical properties, PVDF and other polymers also have a low Curie temperature which is the temperature at which materials lose their magnetic properties or undergoes a sharp change in their magnetic properties. This leads to the development of new ceramic/polymer composites.

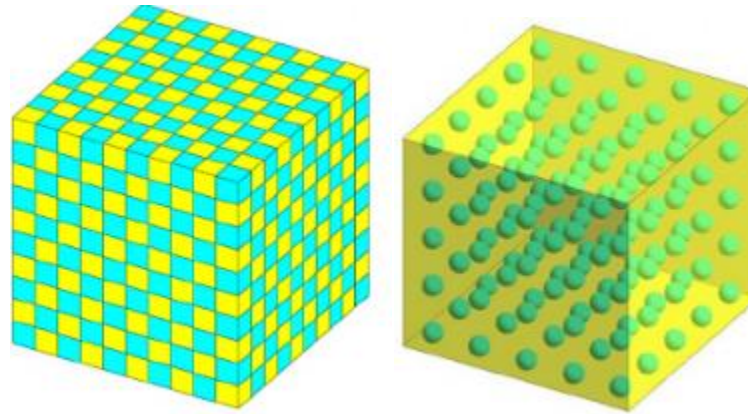


Figure 8.0-3 Particle distribution in a composite [24].

PVDF and PZT both have their advantages and disadvantages. To optimize the performance of the sensor, the combined properties of both the ceramic and the polymer is utilized. Composites are multiphase materials which show the properties of both constituents.

They are composed of two phases: matrix phase and dispersed or discrete phase. Dispersed phase refers to the distribution or orientation of particles of one constituent and matrix phase surrounds the dispersed phase to make a continuous medium. The electromechanical properties of the composite depend upon the connectivity of these phases [25]. Skinner and Newnham [26] first developed the connectivity concept, and currently, there are ten different connectivity patterns depending on which new composites are developed with improved piezoelectric properties. Figure 8 shows one of the commonly used connectivity patterns (0-3) [27] for fabricating a PVDF/PZT composite. The first digit in (0-3) describes the connectivity of the dispersed phase in zero dimensions and the second digit describes the connectivity of the matrix phase in three dimensions. PVDF/PZT composite combines the properties of PZT, i.e. high coupling factor and high dielectric coefficient, and the properties of PVDF, i.e. low acoustic impedance and high flexibility, to create a low acoustic impedance, high coupling factor, medium dielectric constant and flexible composite substrate. Additional piezoelectric properties of PVDF and PZT-5H [28] are listed in Table 2 below:

Table 2: Mechanical and piezoelectric properties of PVDF and PZT-5H [28].

Properties	Symbol	PVDF	PZT -5H (Navy type 6)	Units
Density	ρ	1.76	7.5	kg/m ³
Young's modulus	Y_{11}^E	2-2.5	60.6	$\times 10^9$ Pa
	Y_{33}^E	2-2.5	48.3	$\times 10^9$ Pa
Poisson's ratio	ν	0.29	0.39	
Shear Modulus	G	3.5	2	$\times 10^9$ Pa
Longitudinal wave velocity	v_l	2.25	4000	m/s
Transverse wave velocity	v_s	1.41	1680	m/s
Curie Temperature	T_c	120	220	°C

Piezoelectric matrix (at constant strain S)	e_{13}^S	0.069	-6.5	C/m ²
	e_{23}^S	0.069	-6.5	C/m ²
	e_{33}^S	-0.099	23.3	C/m ²
	e_{42}^S	-0.069	17	C/m ²
	e_{51}^S	-0.081	17	C/m ²
Relative permittivity matrix (or dielectric constant)	ϵ_{11}	-0.268	15.05	$\times 10^{-9}$ F/m
	ϵ_{22}	-0.270	15.05	$\times 10^{-9}$ F/m
	ϵ_{33}	-0.332	13.02	$\times 10^{-9}$ F/m
piezo electric charge coefficients	d_{31}	21	-274	$\times 10^{-12}$ C/N
	d_{32}	2.3	-274	$\times 10^{-12}$ C/N
	d_{33}	-26	593	$\times 10^{-12}$ C/N
	d_{15}	-27	741	$\times 10^{-12}$ C/N
	d_{24}	-23	741	$\times 10^{-12}$ C/N
piezoelectric voltage coefficients	g_{15}		29.9	$\times 10^3$ m ² c ⁻¹
	g_{31}	0.20	-9.3	$\times 10^3$ m ² c ⁻¹
	g_{33}	0.30	18.4	$\times 10^3$ m ² c ⁻¹
Elastic compliance coefficient matrix (constant electric field E)	s_{11}^E	365	16.3	$\times 10^{-12}$ Pa ⁻¹
	s_{12}^E	-192	-5.23	$\times 10^{-12}$ Pa ⁻¹
	s_{13}^E	-209	-7.5	$\times 10^{-12}$ Pa ⁻¹
	s_{33}^E	472	20.3	$\times 10^{-12}$ Pa ⁻¹
	s_{44}^E	472	49.5	$\times 10^{-12}$ Pa ⁻¹
	s_{66}^E	472	43.5	$\times 10^{-12}$ Pa ⁻¹
Coupling coefficients	k_{31}	0.12	-.388	
	k_{33}	0.27	0.752	
	k_{15}		0.675	

1.5. Phases of PVDF

PVDF and its copolymers are known to have superior electroactive properties.

Depending on the arrangement of trans and gauche linkages in the molecular chain of PVDF,

it exhibits five different polymorphic crystalline phases; β (phase I) with TTTT (all-trans) planar zigzag pattern, α (phase II) and δ (phase IV) with TGTG' (trans-gauche–trans-gauche') linkage arrangement, γ (phase III) and ε (phase V) with TTTTGTGTTG' arrangement. It is observed that, despite the same linkage arrangement in α and δ phases, the α -phase PVDF, being hexagonal and monoclinic, contains antiparallel dipole moments which mutually cancel out with each other [29]. This phenomenon is also seen in ε -phase. However, in the β , γ and in the orthorhombic δ phases, the dipole moments orient in the same direction. This configuration of the dipole moment makes α and ε -PVDF non-polar and β , γ , δ -PVDF polar [30, 31]. Apart from the α and ε -phase, all other phases exhibit piezo and pyroelectric properties due to their polar nature. PVDF displays highest dipolar moment per unit cell (8×10^{-30} Cm) in its β phase compared to its α , γ , δ or ε phase. Figure 9 represents the α , γ , δ phases of PVDF.

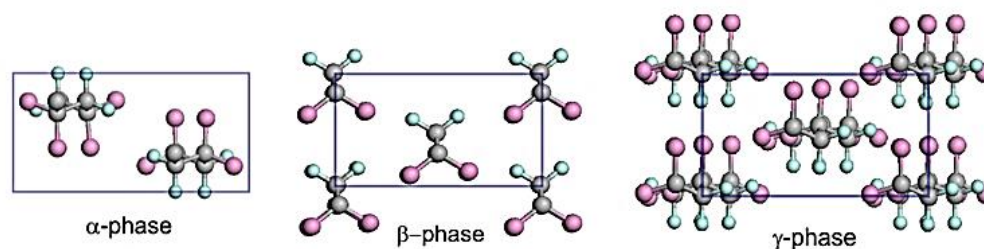


Figure 9. α , β and γ phases of PVDF.

The β -phase crystal has the highest polarity of other crystals due to all-trans conformation and is hence being used extensively in piezoelectric, pyroelectric and ferroelectric applications. Figure 10 below represents the methods to achieve β -phase from α , γ and δ phases.

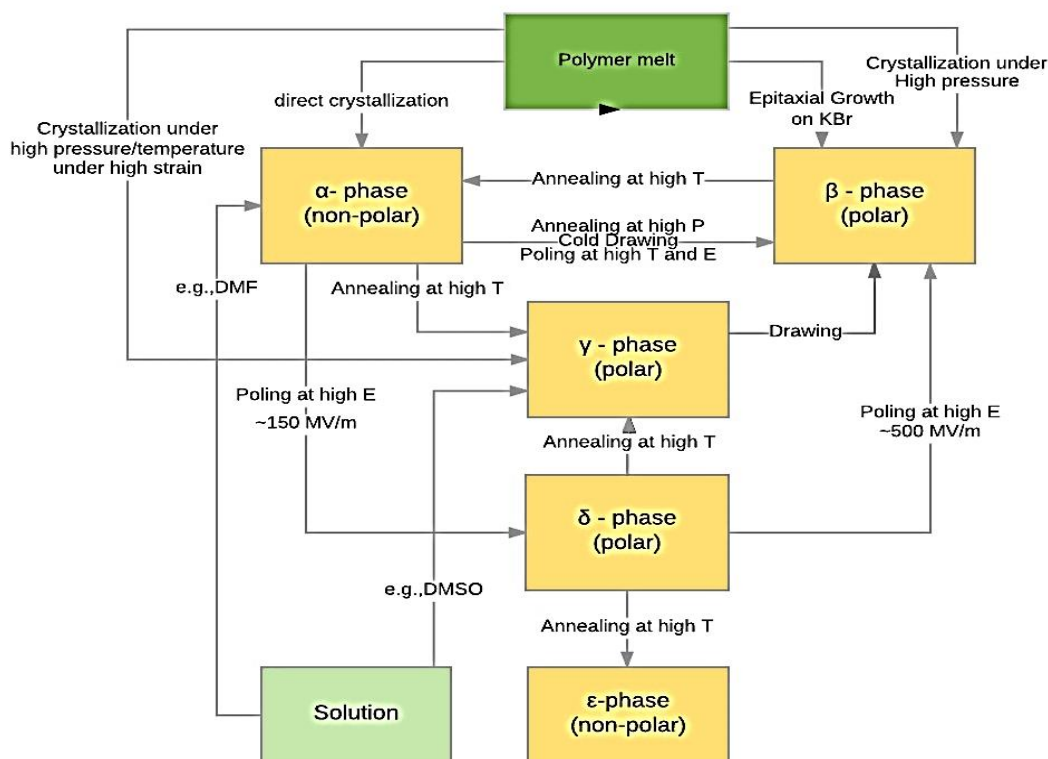


Figure 10. Methods to achieve β phase of PVDF.

It is seen that the β -phase PVDF can be obtained directly by crystallization of the polymer melt at high pressure or by direct crystallization to obtain α -phase, which can then be annealed at high pressure or cold drawn/stretched and poled at high temperature and electric field to obtain the β -phase. Also, crystallization of polymer melt under high temperature and pressure leads to γ -phase, which could be drawn to β -phase [32, 33]. Poling α -phase PVDF at a high electric field of 150 MV/m could lead to the formation of δ -phase which when poled at an even higher electric field of around 500 MV/m leads to the formation of β -crystalline phase.

The β phase can also be achieved directly by adding a copolymer P(VDF-co-trifluoroethylene); In this case, polarization is attained merely by applying electric current without being stretched. Also, P(VDF-TrFE) is more crystalline and has higher temperature

stability (up to 100 °C) and thus produces a larger piezoelectric response. Its d_{33} response value is as high as -38 pC/N compared to -33 pC/N in pure PVDF.

Fabrication of 0-3 composites as the substrate material of the SAW device has been performed both with PZT-PVDF and PZT-PVDF-TrFE for comparison of flexibility and ease of fabrication.

1.6. Interdigital Transducer (IDT)

The first successful implementation of IDT in a SAW device after its discovery was given by Tancrrell [34] in 1969 where he incorporated the IDTs onto a lithium niobate substrate. The geometry of the IDT primarily governs the signal processing and frequency response characteristics of the SAW device [35]. This gave rise to different IDT design configurations. IDTs are typically made up of a combination of parallel electrode extending between two rectangular shaped bus bars. Depending on the number of the electrode in a period the IDTs are termed as single, double, or multi-electrode type IDT.

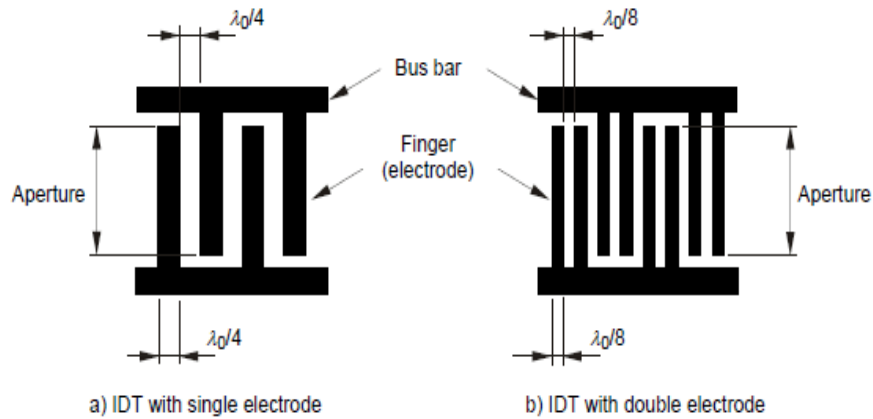


Figure 11. IDT configurations.

In case of double-electrode IDT which is being used in this research, a pair of two electrode pair (IDT fingers) of width equivalent to wavelength λ , each pair connected to the

oppositely placed positive and negative bus bars, is considered as one period. Also, the thickness of each electrode and the spacing between the electrodes is $\lambda/8$. Figure 11 shows a single and double electrode design of an IDT. The ratio of the finger width to the width of the spacing is termed as the metallization ratio, which is an important parameter to be considered while designing the transducer, which in our case is 1. Single-electrode type IDT is simpler and has a wider electrode width when compared to the split or multi-electrode type IDT [37].

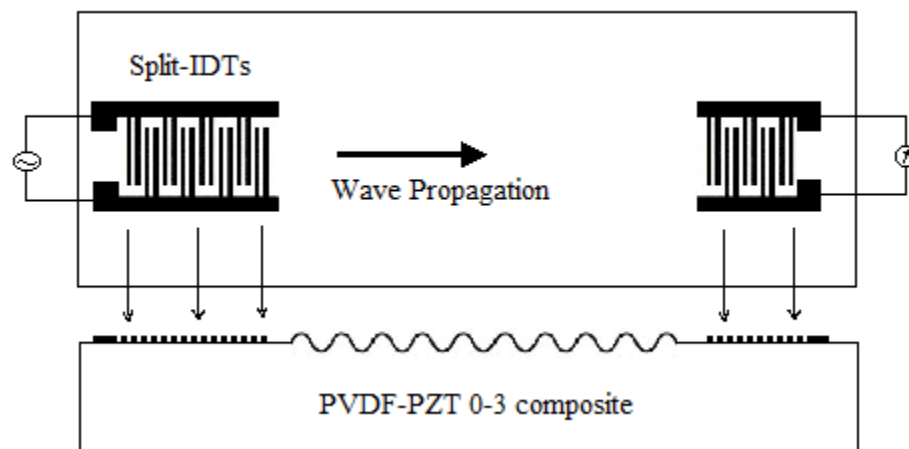


Figure 12. Top and side view of SAW device.

As the IDTs are excited to produce acoustic waves, the waves that propagate on the surface can interact with the transducer edges and result in wave amplitude losses. The waves underneath the transducer fingers are then disturbed. The center of excitation of waves and the center of reflection the waves produced by the transducers are deviated from the normal and could hence alter the systems center frequency, change the transfer characteristics and reduce the filter bandwidth. Single-electrode type IDTs generally favors such reflections and result in such losses. Hence, split or double-electrode type IDTs are preferred where the two adjacent fingers suppress such reflections by destructive interference. Even though double-electrode

type IDTs exhibit asymmetric transfer characteristics [38] they are used in this research to prevent huge losses due to reflection.

1.7. Objectives and Approaches

The primary purpose of the experiment is to fabricate a passive wireless SAW sensor made of a base flexible with integrated IDT which helps in electromechanical wave conversion. PZT (piezoelectric ceramic) and PVDF (piezoelectric polymer) have been chosen as the substrate material to enhance the flexibility of the product and to emit desirable properties (discussed in the introduction) to the obtained composite. Hence a polarized 0-3 composite need to be fabricated comprising of dispersed PZT particles in a copolymer of PVDF matrix to provide good mechanical strength, high electromechanical coefficient, and high dielectric constant to the composite without disturbing the flexible nature of PVDF copolymer. The substrate must be mechanically compressed and electrically polarized at elevated temperature to produce thin samples which can then be cut to the desired shape.

Mathematical modelling of the response of the device must be performed with the incorporation of IDTs. Design parameters, frequency response and other characteristics of the IDTs are to be considered during fabrication. Several device modeling methods are taken into consideration: First Order Impulse Response, P-Matrix, Coupling of Modes (COM) and Transmission Matrix approach. Outweighing the pros and cons for each of these methods, First Order Impulse Response and Second Order Transmission Matrix approach which makes use of the Equivalent Circuit model are studied.

Once the modeling is complete and the required parameters are achieved, the IDTs are to be developed on the surface of the substrate using a conventional photolithographic technique through a series of deposition and etching process.

On fabricating the input and output IDTs, it can be electrically connected to the RF signal and amplified to produce a feedback loop. Strain measurements are to be performed as a measure of the shift in the frequency of the SAW device.

2. SAW Device Modelling

2.1. Working Principle

The basic operation of a passive SAW sensor involves connecting the input IDT to an antenna at which an RF pulse is received. The RF interrogator or receiver sends out a signal. The signal is captured by an IDT consisting of a series of comb-like structures with a pattern that resembles fingers. The input IDT generates an electric field with a frequency that can be determined by the gap between two adjacent fingers of the IDT. The field then creates an acoustic wave across the substrate utilizing the piezoelectric effect. The output transducer senses the incoming electric field that accompanies the acoustic wave through the inverse piezoelectric effect. The antenna further receives the interrogation signal. The signal is then demodulated and is subjected to signal processing to extract the RFID and other information from the sensor [40,42]. Figure 13 shows the schematic of how RF waves are transmitted and received in a SAW sensing system.

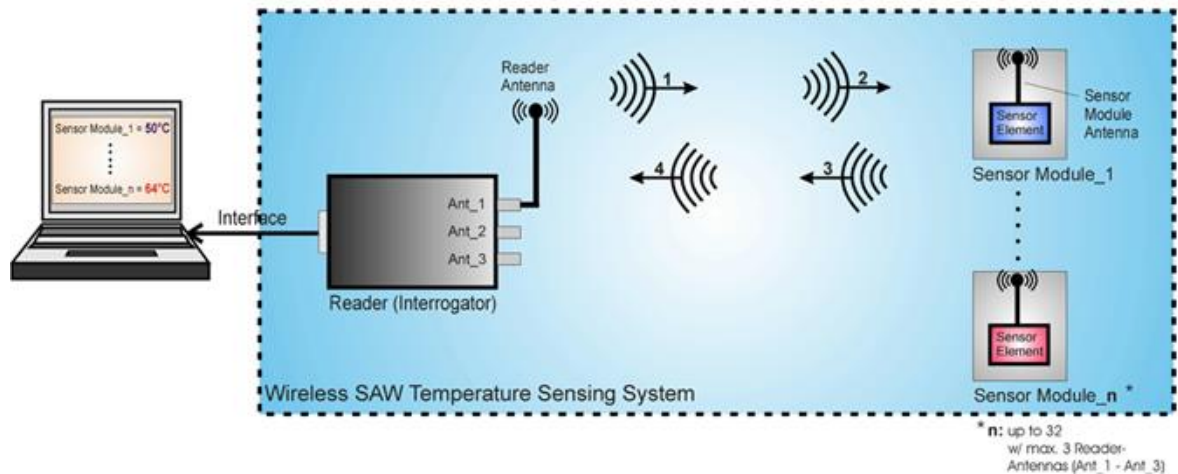


Figure 13. Interrogation of several SAW sensors simultaneously [39].

2.2. Design Parameters

As mentioned, one of the main components of a SAW sensor is Interdigital Transducer (IDT). Modelling of IDT determines the frequency response characteristics of the SAW device. The electrodes of IDT are mainly placed in-plane to the substrate to build up capacitance associated with the applied electric field which penetrates below the substrate surface.

When a voltage is applied across both the busbars, an electric field is generated which travels through the fingers. Since each electrode pair is made up of a combination of positive and negative electrodes, the region between the fingers accumulates charge and produces the electric field in these regions. Due to the electric field, the finger spacing experiences periodic expansion and compression creating strain [43]. The strain thus generated from the individual period adds up to form a larger wave (called surface acoustic wave) which propagates from the end of the input IDT and travels both in a longitudinal and transverse direction to the SAW device. The waves produced during each period when averaged is considered as that excited from the center of the IDT (called the excitation center) due to the symmetry of the fingers. Figure 14 shows the direction of motion of positive and negative IDT fingers when the electrodes are excited with an electric field.

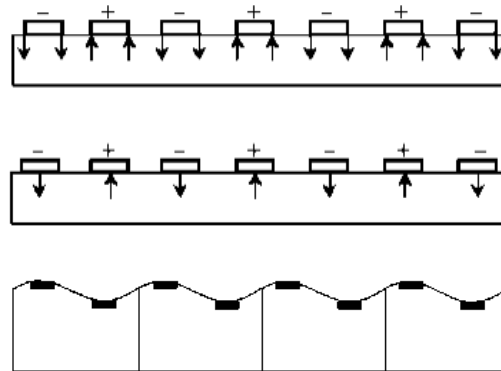


Figure 14. Wave generated by IDT fingers excitation [44].

The frequency of the waves propagating on the surface of the PZT-PVDF/ PZT-PVDF-TrFE 0-3 composite substrate is dependent on the spacing between the IDT fingers. Also, the Rayleigh wave-based SAW sensors concentrate wave energy within one wavelength [45] depth from the substrate surface. When the excitation frequency of IDTs is changed, the acoustic wavelength changes which in turn varies the depth of energy concentration from the substrate surface in a linear fashion. The wavelength λ of the surface acoustic wave is related to the SAW frequency f_0 and the acoustic velocity v in the media [46] by:

$$\lambda = \frac{v}{f_0} \quad (3)$$

SAW waves are dispersive in nature. Within a frequency range of 5 to 100 MHz the acoustic velocity changes by several hundred.

Fractional bandwidth of the SAW device is measured by its resonant frequency concerning its null bandwidth and is denoted by 'B.'

$$B = \frac{NBW}{f_0} \quad (4)$$

Where NBW is the null bandwidth

The Width of the finger measured concerning its acoustic wavelength for the double IDT is given by $\lambda/8$ and the interdigital spacing measured from the center – to – center between two fingers is $\lambda/8$, and finally, the number of finger pairs needed to achieve the fractional bandwidth is

$$N_p = \frac{2}{B} \quad (5)$$

The Aperture or Overlap between fingers depends on the total capacitance of the IDT system. It is denoted by ' C_t' '.

$$C_t = \frac{1}{2\pi f_o Z} \quad (6)$$

Where Z is the impedance of the IDT which should match the impedance of measurement system for best response, and the Aperture or Overlap between fingers is given by:

$$W = \frac{C_t}{C_o N_p} \quad (7)$$

Where C_o is the capacitance per finger pair per unit length.

Finally, the magnitude frequency response is approximated as an incoherent addition of individual finger contributions and given as

$$\varphi(f) = \left| \frac{\sin X}{X} \right| \quad (8)$$

Where

$$X = \frac{N_p \pi (f - f_o)}{f_o}$$

To design and simulate an IDT very accurate tools have to be used. Various research has been performed to design the IDT to obtain high efficiency, and hence several models were proposed depending on the order of model accuracy. These include the signal theory such as the impulse response model, the field theory such as the Finite elemental modelling, Greens function and so on, and the network theory such as equivalent circuit model, P-matrix model, the coupling of modes theory (COM) model, the cross-field model (Transmission matrix approach), and the angular wave spectrum model [47].

2.3. Impulse Response Model

Impulse response model gives the first order approach for modeling the piezoelectric, mechanical and electrical behavior of the SAW device [48]. It provides a simpler way of determining the IDT specifications and the wave parameters by relating the IDT finger location with the signal generated as the acoustic wave's impulse the IDT finger while traveling below it. This method takes very less computational time by calculating the Fast Fourier Transform (FFT) of the raw signal. This model ignores the second order effects such as reflections, dispersion, wave diffractions, and charge distribution. Also, it assumes that one or both IDTs are uniform apodized (constant variation in the overlap finger length) and must have a constant finger width, thus simplifying the calculations [49].

The frequency response of the SA

W device using Impulse Response method is given by:

$$|H(f)| = 2k\sqrt{(C_t f_0)} N_p \frac{\sin X}{X} \quad (9)$$

The total admittance for the model is calculated to ensure the maximum current flow at the maximum operable frequency and to check the signal match of electronic feeding system to that of the structure. It is given by combining by superposing the real part which is radiation conductance and the imaginary part which is acoustic susceptance.

$$Y = G_a + j(2\pi f C_t + B_a) \quad (10)$$

Where G_a the radiation conductance, f is the frequency range and B_a is the acoustic susceptance.

Insertion loss is also calculated from the model; it determines the losses from the IDT, propagation losses and reflector losses if applicable. It is calculated as the logarithmic ratio of the power delivered to the load impedance before the SAW device is inserted to the power delivered to the load impedance after it is inserted.

$$IL(f) = -10 \log \frac{2G_a(f)R_g}{(1 + G_a(f)R_g)^2 + [R_g(2\pi f C_t + B_a(f))]^2} \quad (11)$$

Where R_g is the load resistance.

2.4. Coupling of Modes (COM) Theory

The coupling-of-modes (COM) theory models SAW device responses more accurately by considering the internal transducer reflections and providing the nature of reflectivity and power transduction within a transducer [50]. Two waves traveling in the opposite direction is assumed to be linearly coupled to their amplitude, voltage, and current. It also assumes that in periodic structures, only the coupling between the strong incident and reflected wave occurs.

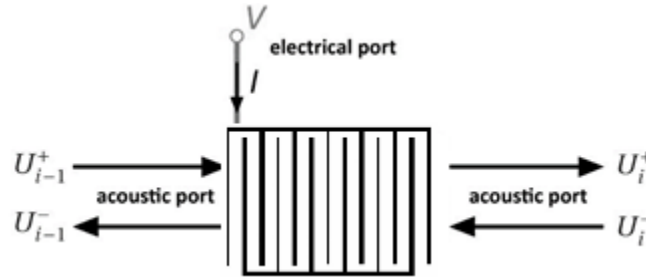


Figure 15. 3-Port representation of an IDT.

The COM equations were represented by a P-matrix method developed by Tobolka [81] in 1979. This is a very accurate model requiring a limited number of physical parameters to analyze a device. It provides a 3-port representation for each finger of an IDT of which the two ports are acoustic, and one is electrical [51]. Figure 15 shows the 3-port representation of an IDT. It provides a cross-field equivalent circuit representation for each finger to produce a mixed matrix whose coefficient depends on the COM parameters, such as reflectivity, velocity, capacitance, and wave attenuation and transduction coefficient. The acoustic ports are represented by a SAW scattering matrix (S-matrix), and the electric ports are described by an

admittance matrix calculated for each finger and then for the entire transducer geometry, thus providing an overall transfer function of the SAW device.

2.5. Equivalent Circuit Model

Equivalent circuit model, such as the Masons model, is another approach similar to the P-matrix representation used for design modeling. It gives an equivalent electrical circuit representation of the electromechanical system and uses device properties, such as wave velocity, center frequency, electromechanical coupling coefficient and null bandwidth. This allows designers to determine the major dimensions and parameters in the SAW device, such as the number of fingers, finger width, and finger aperture, length of the delay line, frequency response, impedance parameters, and transfer characteristics of SAW device [52].

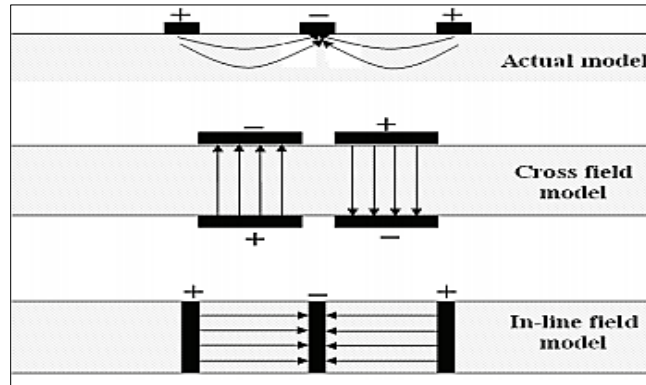


Figure 16. Side-view of interdigital transducer showing the field patterns.

It uses a 3-port electrical representation like the P-matrix ports, where two ports are the electrical equivalent of the two acoustic ports, but the third port is an actual electrical port where input and output signals could be applied and detected. Hence this method simulates a coupling between both electro-mechanical system and mechano-acoustic system to provide

admittance value for a single finger and a finger pair and then generate an overall admittance with the transfer function for the whole IDT [53].

On converting the IDT into an electric representation, the device can be analyzed as a one-dimensional model. This simplification is feasible since the assumed vibration can be taken as a one-dimensional longitudinal wave propagation. Figure 16 shows the field patterns of an IDT where we can observe the actual model and two approximations: Crossfield and In-line field. Mason's equivalent circuit is not feasible due to the presence of a negative capacitance in the circuit. This is observed in the in-line model where the direction of the wave propagation is parallel to the excitation field. However, this negative capacitance could be avoided by a cross-field model technique where the Rayleigh waves excited in the direction perpendicular to the excitation field.

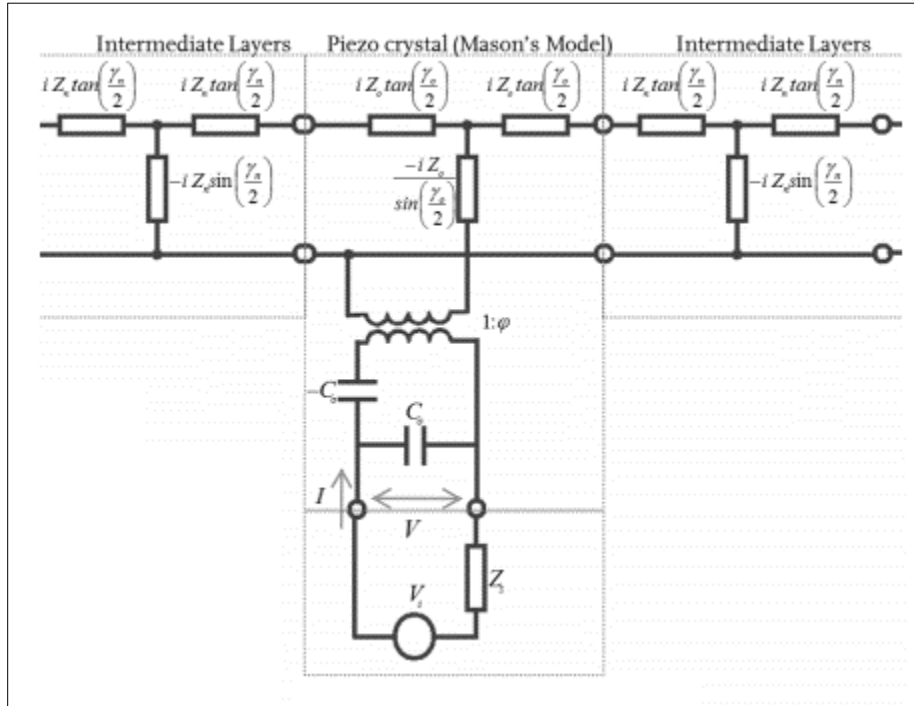


Figure 17. Mason's equivalent circuit for one finger of an IDT in cross-field approximation [54].

Masons equivalent circuit [55] consists three lumped elements that are transcendental functions of frequency necessary to take acoustic wave propagation in the crystal into consideration. It divides an IDT into zones of half wavelengths with the metalized region under the IDT taken as $\lambda/4$ and the un-metalized region of $\lambda/8$ taken under both sides of the IDT. Figure 17 shows the Masons equivalent circuit for one finger of an IDT where the lumped elements of the free region are on either side of the lumped elements of the metalized region in cross-field approximation.

2.6. Transmission Matrix Approach

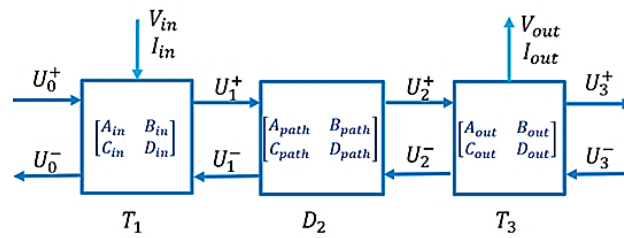


Figure 18. Block structure of SAW delay line sensor.

Transmission matrix is a second order modeling approach that makes use of an equivalent circuit model and considers the second-order effects: reflections, wave diffractions, charge distributions and dispersion. It makes use of previously established approaches: P-matrix, COM and traditional matrix, however, this modified transmission matrix approach can cascade acoustic and electric fields in both series and parallel connections. Similar to COM and P-matrix approaches, it considers the IDT as a 3-port device and the matrix of the whole device is a 3x3 transmission matrix [56]. Figure 18 shows the block structure of the SAW delay line sensor. The basic principle in calculating the transmission matrix for the whole IDT is

based on [ABCD] transmission line theory given in equation (12) which relates the amplitudes of the forward and backward traveling waves.

$$\begin{bmatrix} A_{device} & B_{device} \\ C_{device} & D_{device} \end{bmatrix} = \begin{bmatrix} A_{in} & B_{in} \\ C_{in} & D_{in} \end{bmatrix} \begin{bmatrix} A_{path} & B_{path} \\ C_{path} & D_{path} \end{bmatrix} \begin{bmatrix} A_{out} & B_{out} \\ C_{out} & D_{out} \end{bmatrix} \quad (12)$$

Moreover, the transmission matrix for the IDT from the 3-port network observed in Figure 18 s:

$$\begin{bmatrix} U_{i-1}^+ \\ U_{i-1}^- \\ I_i \end{bmatrix} = \begin{bmatrix} t_{11} & t_{12} & t_{13} \\ t_{21} & t_{22} & t_{23} \\ t_{31} & t_{32} & t_{33} \end{bmatrix} \begin{bmatrix} U_i^+ \\ U_i^- \\ V_i \end{bmatrix} \quad (13)$$

The overall transmission matrix is achieved by cascading the transmission matrix for each finger which involves using the equivalent circuit to calculate the ABCD parameters, impedance, and voltage and phase angle for free and metalized regions of the finger shown in equation (1) [57]. Figure 19 shows the side view of free and metalized regions for a single finger. The impedance value below the finger is different from that below the free region.

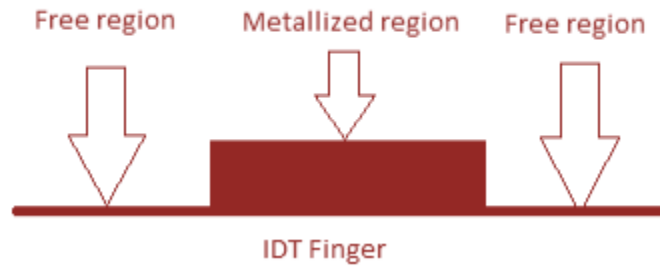


Figure 19. Schematics of a single finger of IDT in side-view [58].

Once the transmission matrix for a single finger is calculated, the equation is cascaded for N number of fingers. In case of double electrode design, the matrix is calculated for a finger pair and then cascaded for N finger pairs. The transmission matrix for delay line is calculated and given by:

$$[D] = \begin{bmatrix} e^{j\beta d} & 0 \\ 0 & e^{-j\beta d} \end{bmatrix} \quad (14)$$

Now, the final transmission matrix for the whole device is calculated by cascading the input IDT transmission matrix, the delay line transmission matrix and the output transmission matrix from which the frequency response and Y or admittance parameters are calculated [59].

One of the assumptions made for developing these equations is that wave absorbers are placed on either side of the device, therefore, the boundary conditions are: $U_0^+ = 0$ and $U_3^- = 0$.

As previously described in the P-matrix approach, the SAW sensor comprises one electrical port computed by the admittance or Y-matrix and two acoustic ports calculated by the scattering or S-matrix approach. Due to the symmetry of the acoustic ports about the electric ports, the admittance matrix is represented as in equation (15).

$$[Y] = \begin{bmatrix} Y_{11} & Y_{12} & Y_{13} \\ Y_{12} & Y_{11} & -Y_{13} \\ Y_{13} & -Y_{13} & Y_{33} \end{bmatrix} \quad (15)$$

The variation in sign ensures that there is a symmetric flow of acoustic waves from the input to output port.

S-matrix, on the other hand is a complex square matrix where the S-parameters are to be calculated to study the high-frequency transmission and reflection characteristic of the delivered signal in the frequency domain. Equation (16) represents the relationship between voltage and current combined by the S-matrix:

$$\begin{bmatrix} I_{in} \\ I_{out} \end{bmatrix} = \begin{bmatrix} S_{11} & S_{12} \\ S_{21} & S_{22} \end{bmatrix} \begin{bmatrix} V_{in} \\ V_{out} \end{bmatrix} \quad (16)$$

Where

$$S_{11} = \left. \frac{I_{in}}{V_{in}} \right|_{V_{out}=0} \quad \text{is the input port voltage reflection coefficient or return loss}$$

$$S_{12} = \left. \frac{I_{in}}{V_{out}} \right|_{V_{in}=0} \quad \text{is the reverse voltage gain or transmission isolation}$$

$$S_{21} = \left. \frac{I_{out}}{V_{in}} \right|_{V_{out}=0} \quad \text{is the forward voltage gain or transmission insertion loss}$$

$$S_{22} = \left. \frac{I_{out}}{V_{out}} \right|_{V_{in}=0} \quad \text{is the output port voltage reflection coefficient}$$

3. Fabrication and Testing

3.1. Fabrication

SAW sensor fabrication is divided into three subgroups: fabrication of the composite, poling of PZT-PVDF/ PVDF composite and development of IDT.

3.1.1. Preparation of Composite Substrate

To improve the dielectric and piezoelectric response, PVDF/PVDF-TrFE are separately combined with a highly piezoelectric ceramic PZT in a 0-3 type composite manner. PVDF has good mechanical property and is highly flexible. This when combined with PZT, having excellent piezoelectric properties, forms a ceramic-polymer composite which is ideal for piezoelectric applications. It is required to maintain an optimum amount of ceramic content in the polymer matrix due to the constraints in the mechanical properties of the film. Higher content of ceramic grains results in reducing the connectivity between ceramic and polymers.

One concern about PVDF is its hydrophobic nature [60] which makes it incapable to adhere to substances dissolved in water. Tests have been conducted to improve the hydrophobicity of PVDF. Results have shown that doping the PVDF membranes with inorganic Nano-particles like Al₂O₃, ZrO₂, TiO₂, and SiO₂ increased the hydrophilicity and permeability and reduced membrane fouling. An alternative approach to dissolve PVDF is by using a polar solvent. Predominant β phase is achieved by the addition of strong polar solvents having high boiling points and low evaporation rates, such as N, N-Dimethylformamide (DMF), N-methyl-2-pyrrolidone (NMP), dimethyl sulfoxide (DMSO), dimethylacetamide (DMAc) [61]. Addition of these solvents affects the porosity of the PVDF film due to their low evaporation rates. Increased porosity could prevent PVDF film from exhibiting electrical

properties. Hence the selection of solvent plays a major role in achieving β -phase crystallization with fine film porosity and in turn provide good mechanical strength [62].

Methods employed to prepare the composite substrate includes injection molding, lamination, laser or ultrasonic cutting, di-electrophoresis, co-extrusion, solvent casting, hot pressing, and spin coating method. However, since we had easy accessibility to the hot-pressing machine, we decided to use the machine to produce a thin composite film.

PVDF and in the form of powder with average molecular weight $M_w \sim 534,000$ g/mol and density of 0.944g/ml was bought from Sigma Aldrich.

Fabrication steps are written only for the PVDF-PZT composite. Similar steps are followed for both PVDF and its copolymer. The substrate is fabricated [63] in the following process:

- a) 20 wt.% of PVDF (3.85g) powder was weighed using a digital balance.
- b) 80 wt. % DMSO (15 ml) was measured using a pipette and added to the PVDF powder. The wt% of DMSO in grams was simply calculated from its density (0.944g/ml).



Figure 20. a) Weighing PVDF using a digital balance, b) Measured PVDF powder.

- c) To obtain a uniform mixing of the PVDF sample in DMSO, the sample was stirred mechanically using a magnetic stirrer and subjected to heating on a hot-plate at about 50-60°C for 45 minutes.
- d) This mixture was then subjected to ultrasonification to obtain a uniform distribution of the powder in the solvent until an optimum viscosity for adding the ceramic powder is achieved.

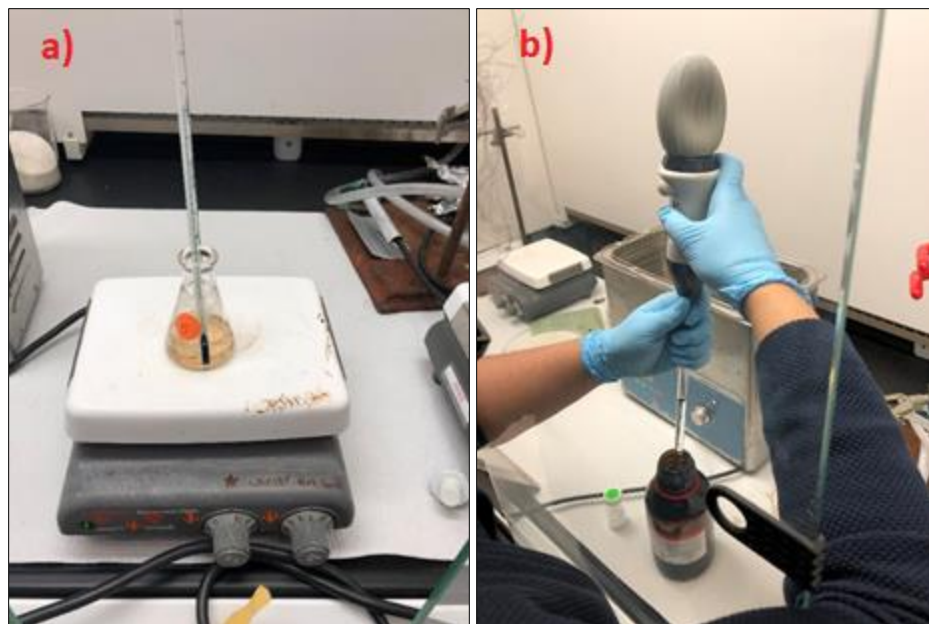


Figure 21. a) Measuring DMSO, b) Heating the PVDF-DMSO mixture.

To remove lumped masses, a mesh size of 38 microns was used to sieve the PZT powder.

- e) 50% of PZT(5.2g) ceramic powder was added to this solution and was stirred mechanically for about 6-12hr.
- f) It was then subjected to ultrasound again for 30 minutes until the ceramic powder was uniformly distributed in the polymer solution. The inorganic solvent in the mixture was let to evaporate completely in an oven for about 35-45 minutes until the mixture coagulated at around 100°C.

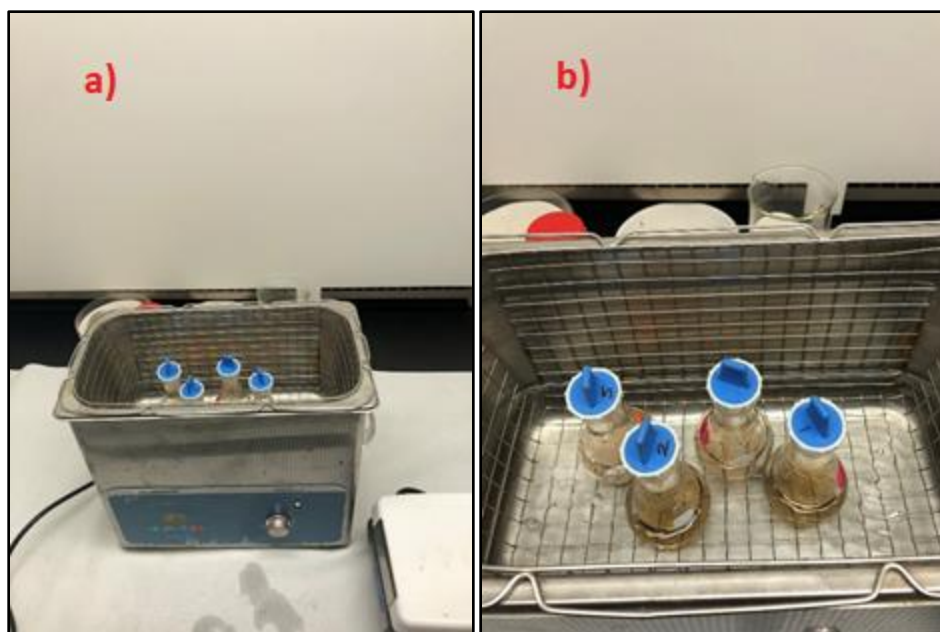


Figure 22. a) and b) PVDF-PZT-DMSO mixture subjected to ultrasound.

g) This coagulated mass was then subjected to hot-pressing at the crystallization temperature of the polymer of about 180°C and pressure of $0.5 \times 10^6 \text{ N/m}^2$ for about 15 minutes.



Figure 23. a) Oven heating of the solution to evaporate DMSO b) Hot-pressing the dried mass.

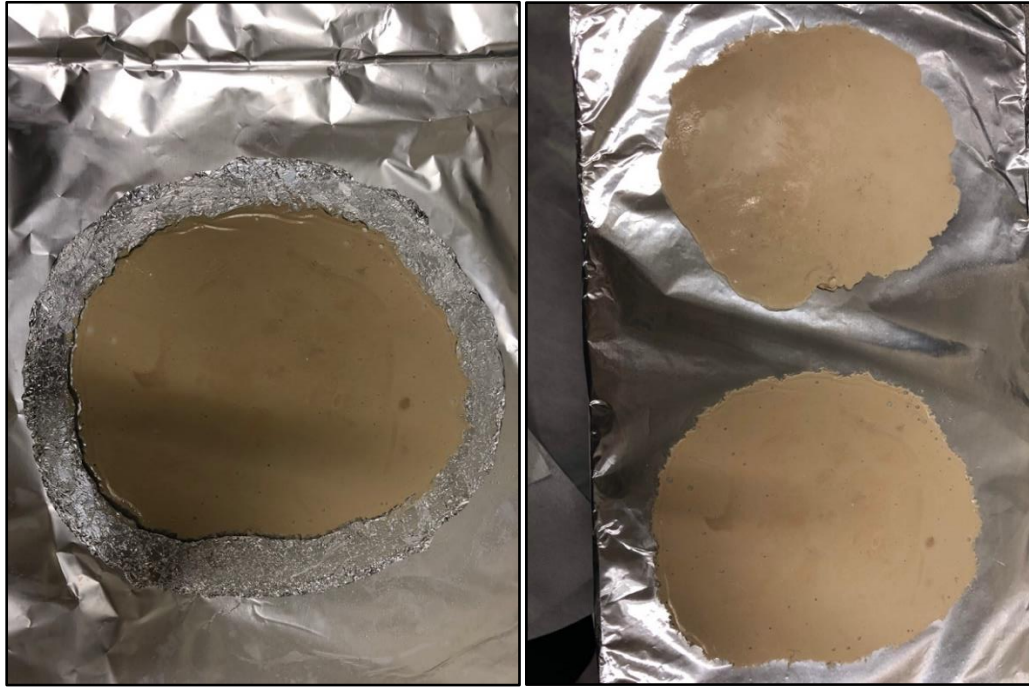


Figure 24. PVDF/PZT sample cooled to room temperature and let dry for a day to get the flat round composite.

To adjust the thickness of the sample, a roll of Al foil was placed around the sample during hot pressing [64]. Hot pressing results in the formation of a disc-shaped mold diameter about 10 cm. The thickness of the mold ranged from 0.5-0.9 mm depending on the cavity and pressure provided. It was then cut to different dimensions such as 4x4cm, 3x3cm and 3x1cm dimension as a varying surface area for IDT incorporation.



Figure 25. a) PVDF/PZT 0-3 Composite after it is cut.

The surface of the substrate showed traces of coagulated mass generated during uneven oven heating in the Petri-dish. This can be avoided by using a Petri-dish with a flat base which helps in uniform heating of the liquid material at every point and could then be subjected to hot-pressing.

A flexible substrate was thus generated with PVDF/PZT composite which was capable of being bent many times without producing any cracks or other kinds of damages. This substrate could then be subjected to a micro gold sputtering which in total would remain flexible. Figure 24 shows the bulk substrate material cut with 3 cm x1 cm dimension and their flexibility.

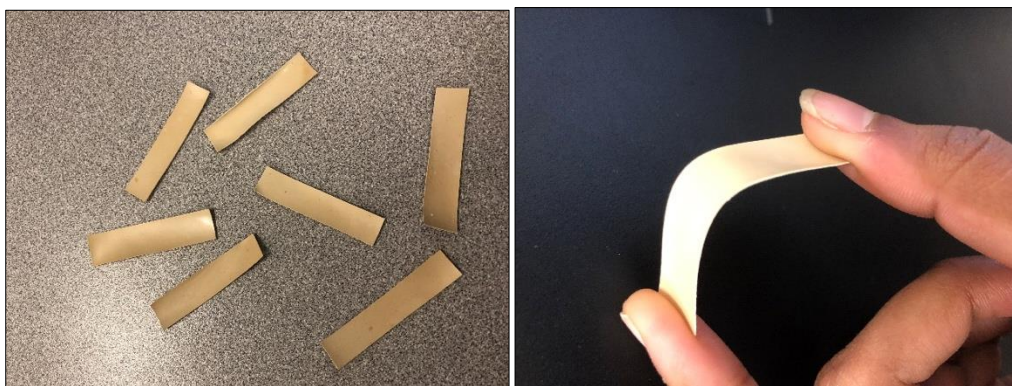


Figure 26. Flexible sensor substrate.

Thus, the result produced a uniform distribution of PVDF particles in the solvent. It was seen during the experiment that adding 50% of PZT powder to the solution made the final product exhibit good piezoelectricity maintaining flexibility.

DMF was initially used in the research as the solvent for PVDF. But due to the hazardous nature and exposure to human, the usage of the chemical was limited. DMF is classified as a carcinogenic chemical and can also produce a reproductive toxin which could eventually damage a developing fetus while DMSO is hepatotoxic and will not cause any reproductive problems [65].

DMSO was used in the research to obtain a stable perovskite device. Both DMSO and DMF have excellent solubility property and are from the same class of dipolar aprotic solvent. They have high boiling points of 154°C and 189°C respectively. Also, DMSO/DMF must be completely removed during the evaporation of the final solution in the oven. To remove the excess solvent, toluene and chlorobenzene are generally used.

Hot-pressing is usually conducted when a bulk sample is considered, but due to the limited material available, it was conducted with reduced quantity. Pressing the sample can produce a dense film which increases the piezoelectric property of the film. Also, it has been reported that hot-pressing method is one of the most reliable methods for the fabrication of 0-3 composites since it can operate at high temperature, above the melting point of PVDF (170°C), at the required pressure. When the sample was pressed at 180°C, stretching operation occurs which helps in the conversion of alpha phase to the beta phase.

3.1.2. Poling of the Composite

Poling mechanism must be performed on any piezoelectric sample to induce piezoelectricity and make it usable. In the case of PVDF, the orientation of the dipole

concerning the carbon backbone to which it is attached determines its piezoelectric nature. The negatively charged Fluoride atoms are strongly coupled with the positively charged hydrogen atoms. Since the all-trans β phase has a highly polar arrangement of fluorine and hydrogen atoms, when poled, align the charged hydrogen and fluorine atoms in a unit cell generating a net polarization. The dipoles along the carbon backbone align to produce maximum spontaneous polarization within the crystal. The strong dipole produces a net charge within the β crystal phase. In the absence of such dipoles, there is no charge produced in the β phase PVDF. In the α phase, the dipoles are disorganized within the unit cell, making it non-polar and hence electrically inactive [66].

Poling process [67,68] can be performed by several methods such as thermal, electronic beam poling, electric field, corona, plasma, and hysteresis poling.

Steps undertaken in poling

Step 1: Gold sputtering

Gold was sputtered over the sample as shown in Figure 27 to a thickness of about 0.2 μm using a halogen source for 40 secs on both sides of the substrate.



Figure 27. Shows the gold sputtered samples.

During sputtering, the thickness of the coating is influenced by distance from the target, distance from the center of the stage as well as sputtering time. Apart from its usage in polarization, sputtering gold was also used for

- h) better conduction during scanning electron microscope imaging.
- ii) as an IDT material, where the region around the IDT would be etched away.

Step 2: Thermal Poling

The Polarization of the sample is necessary to impart piezoelectric property to the obtained composite for transduction of electric energy to mechanical energy in a SAW device. The gold sputtered substrate was sandwiched between two copper plates. It was made sure that the dimension of the copper plate was made a few millimeters smaller than the substrate on each side to prevent arcing during polarization. There were no bonding materials applied between the copper plates and the substrate. The plates were held to the substrate by 4

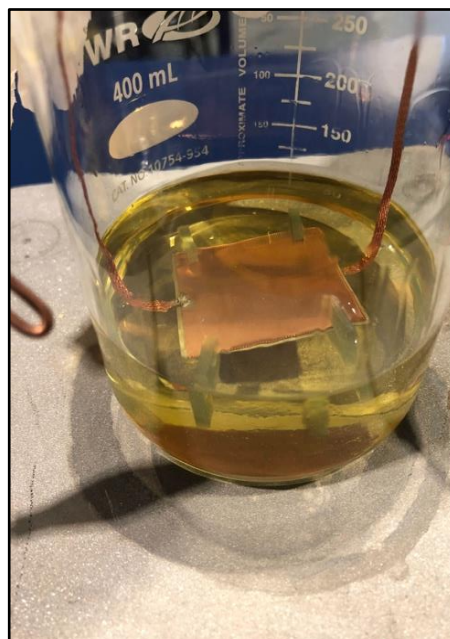


Figure 28. Immersed substrate in Si oil bath for polarization.

small insulated clips which helped the sandwiched member prevent dislocation of layers. Figure 28 shows the process of thermal poling conducted for a 4cm x 4cm substrate material immersed in a silicone oil bath maintained at 110 °C in a glass beaker. The sample was connected to the electric terminals and a DC voltage of about 20 kV/mm was applied in the thickness direction for 1 hour. This process enabled the substrate to obtain the maximum dipole alignment in the thickness direction. Figure 29 shows the polarization process.

The Polarization of PZT occurs if the applied field is higher than the coercive field of PZT. For a 50/50 vol %, PZT/PVDF the piezoelectric charge coefficient (d_{33}) [69] value is then measured. The dielectric voltage coefficient (g_{33}) is then measured from the obtained d_{33} value.

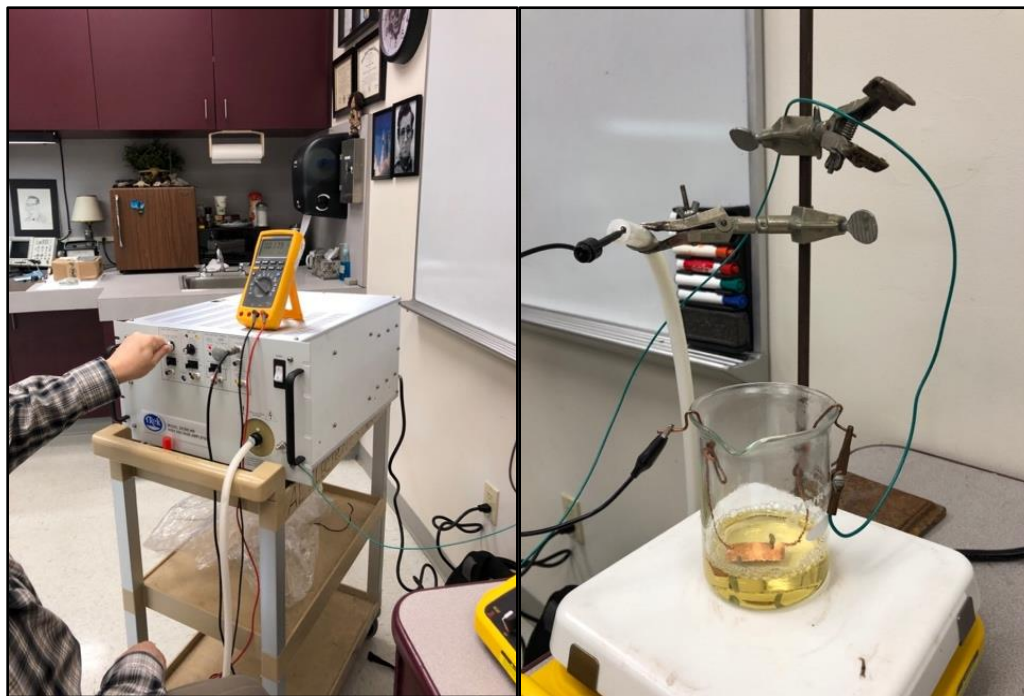


Figure 29. Polarization of PVDF/PZT composite.

3.1.3. Fabrication of IDT

Step 1: Film Deposition

Deposition of film on the composite substrate could be carried out by several techniques depending on the depositions that occur due to chemical or physical reactions. Fabrication of IDTs from chemical mixture includes chemical vapor deposition (CVD), electrodeposition, epitaxy and thermal oxidation and from physical reactions include physical vapor deposition (PVD) and the casting process.

In the CVD process, chemical reactions take place between the source gases enabling it to condense within the reactor as a solid material which then is deposited on the substrate. In case of the electrodeposition process, the substrate and an electrode are placed in an electrolyte, and an electrical potential is applied between the electrode and the conducting area of the substrate [70]. The chemical reaction between the electrodes and the electrolyte helps in depositing a layer of material on the substrate surface. In the epitaxy method, atoms are made to impinge on the substrate surface which subsequently migrates over the surface until they meet other atoms. This forms a two-dimensional flat surface on the surface which grows by incorporating additional atoms to form a complete layer. In case of thermal oxidation, the surface of the substrate is oxidized in an oxygen-rich atmosphere. The film grows into the substrate by diffusion of oxygen, and the process can be accelerated by increasing the temperature to 800° C-1100° C film.

In physical vapor deposition process, materials are deposited onto a substrate by discharging it from the source by either evaporation technique or a sputtering technique.

Casting method [71], used in this thesis, is another form of physical vapor deposition process where the material to be deposited is dissolved in a solvent. In this process, the solution is sprayed or deposited by spinning onto the substrate surface and then the solvent is let to evaporate. This allows a thin layer of material to be coated onto the substrate. This is the common method used mainly on polymer substrates to deposit the photoresist in the process of photolithography. A very thin layer of thickness $<10\text{ }\mu\text{m}$ can be deposited by this technique.

The steps followed in the spin casting process involves:

- a) Dehydrating: substrate sample to dehydrate it above 150 °C for 5 mins.

- b) Spin casting: AZ 1505 photoresist was deposited over the sputtered gold layer of the substrate by spin casting at 500rpm for 10s and then at 3000rpm for the 40s. This allowed a thin layer of 10 μm thickness to be deposited on the substrate. Figure's 30 and 31 show the spin coating process and formation of the photoresist layer respectively.



Figure 30. Spin coating of the sample.



Figure 31. Sample coated with photoresist.

- c) Baking: The coated sample was soft baked in an electric heater at 115 $^{\circ}\text{C}$ for 1 min allowing the photoresist to dry.

Step 2: Pattern formation using photolithography [72]

The photoresist obtained from the spin casting process is covered with a photosensitive mask and is then exposed to a light radiation source of a specific wavelength. The region on the photoresist exposed to the radiation experience a change in chemical resistance properties when a developer solution is sprayed over the photoresist. The region of the photoresist experiencing the change in resistance is etched away by the developer. The unexposed region remains unaltered showing that the material is a positive resist. If the exposed region remains unaltered and the unexposed region etches away, the material is a negative resist. Suitable IDT material is deposited over the resist, and the resist is subsequently etched away by the process called “lift off.” Figure 32 represents the overall fabrication process of the IDT using the photolithography technique.

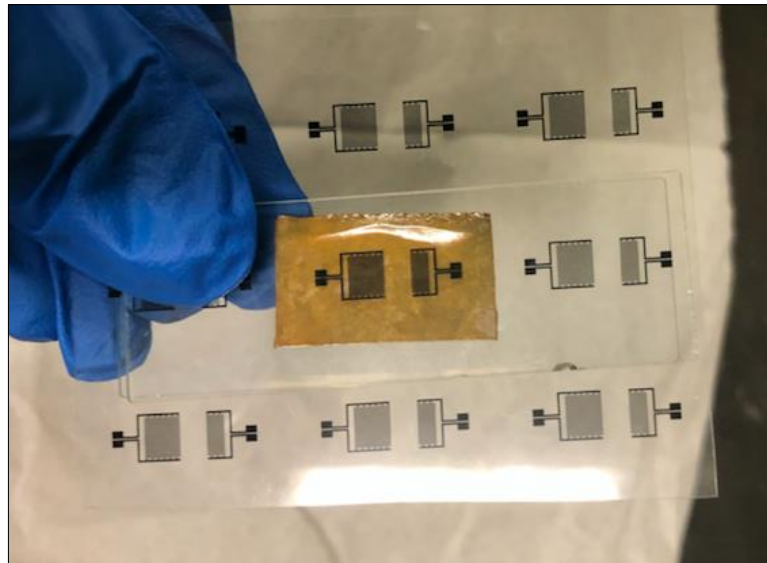


Figure 32. Sample coated with photoresist placed against photomask prepared to be UV exposed.

Figure 33 shows a section of photomask placed over the polarized gold sputtered substrate ready to be subjected to UV exposure. Two glass plates were placed on both sides of

the sample to keep it flat and in contact with the emulsified face of the photomask. The substrate needs to be spin coated to conduct the process of photolithography.

Step 2 was followed in the way described below:

- a) UV exposing: The sample was placed above a glass plate attached to the photomask and was exposed to UV rays of intensity $25\text{mW}/\text{cm}^2$ for 2.7 sec. Positive photomask inhibits the light from reaching the areas on the sample where IDTs are meant to be placed, thus shading the region darker compared to the remaining. Care was taken to conduct this process in a dark room to prevent the photoresist from absorbing unwanted radiations. Figure 33 shows the process of UV exposure on the cut photoresist coated sample.

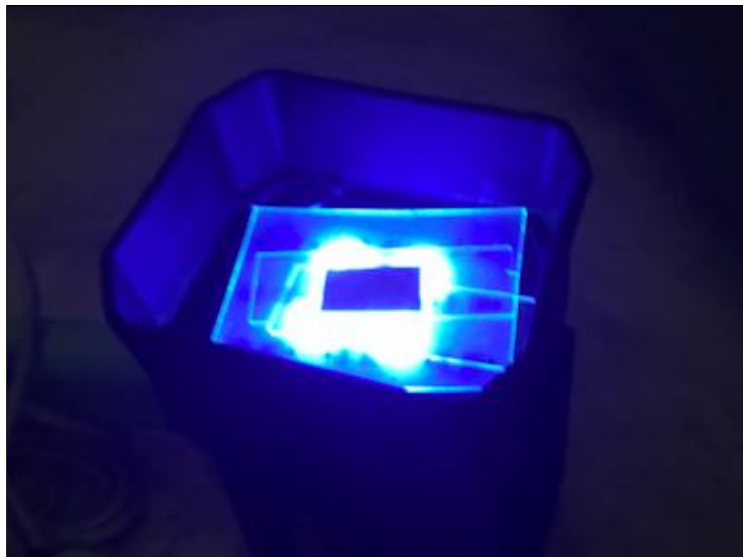


Figure 33. Photoresist coated sample exposed to UV radiation.

- b) Developing: The substrate was then developed to remove the photoresist using AZ 400K developer and leave behind the darker region making it more prominent and visible.
- c) Baking: It was hard baked on the electric heater for 10 minutes at 120°C .

- d) Etching: The sample is then subjected to etching to remove the unwanted region of sputtered gold using the Gold Etchant TFA which completes the process of photolithography where the gold IDTs are thus produced.

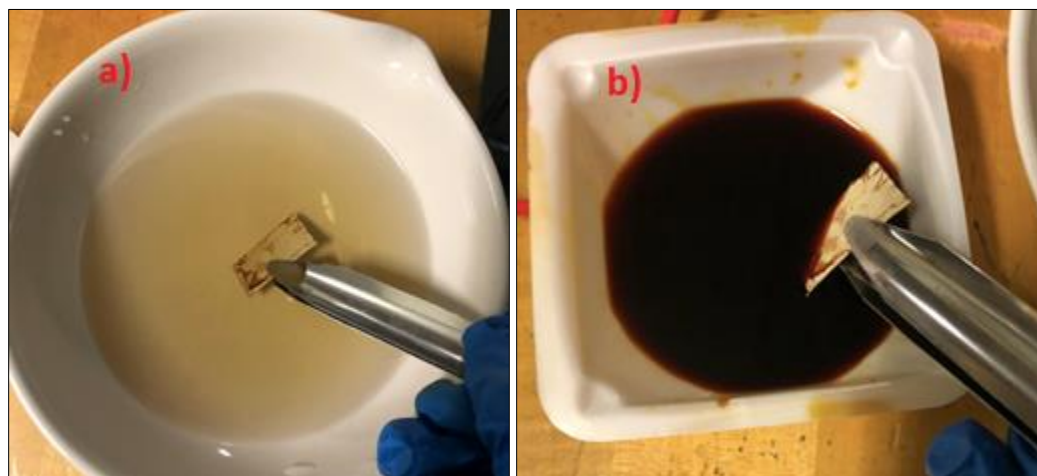


Figure 34. a) Developing the UV radiated sample b) Etching the unexposed gold.

3.2. Testing:

3.2.1. Testing of the 0-3 Composite

3.2.1.1. FTIR scanning graph of PVDF-PZT 0-3 composite

Fourier-transform infrared spectroscopy (FTIR) is a method to determine the infrared spectrum of the absorption and emission/ transmission data of any material. As we know, all materials are made up of molecules that have bonds that continuously vibrates and moves around by undergoing stretch or bend motions [73]. When the frequency of the excitation of these molecules matches with the frequency of the IR radiation, the type of linkages in these molecules can be determined.

FTIR data thus provides the absorbance and transmission characteristics at a wide range of infrared wavelength and shows the peak at a certain wavelength at which the material

absorbs or emits the radiation. The amplitude of the peak depends on the Infrared (IR) absorbance and transmittance capability of the material.

The comparison has been made with the absorbance and transmission characteristics of PVDF, PVDF-TrFE and PZT composite using excel and the analyzed result has been plotted in Figure 35.

Figure 35. Graph comparing the IR absorbance of PVDF, PVDF-TrFE, and PZT.

From the Graph, the absorbance vs. wavelength characteristics of PVDF and PVDF-TrFE are shown with high-intensity peaks in the wavelength range of 400-1750 cm^{-1} . A narrow peak representing highest absorption intensity is shown at a wavelength of 1210 cm^{-1} for PVDF and at 1200 cm^{-1} for PVDF-TrFE depicting the strong C-C bond. Similar narrow high-intensity peaks are shown at 800 cm^{-1} for PVDF and at 810 cm^{-1} for PVDF-TrFE which indicates the asymmetrical stretching vibration in the C-C-C bond and vibrational [74] stretching in the C-F bond. The absorption peak appearing at 1430 cm^{-1} for PVDF and 1400 cm^{-1} for PVDF-TrFE attributes to the CH₂ wagging vibration. Band in the range between 500-800 cm^{-1} represents the M-O-M (M stands for metal) is shown to represent the strong perovskite [75] structure of PZT crystals.

FTIR testing was performed with PVDF-PZT composite only. An absorbance plot for the composite developed from PVDF, DMSO and PZT is shown in Figure 36 as seen from the plot, a combination of DMSO and PVDF is found to have the highest absorbance intensity peaks of up to 0.5 and is absorbed in various frequency band of the IR spectrum with the wavelength in the range of 400-1750 cm^{-1} and in the range of 2600-4000 cm^{-1} .

DMSO is an ambidentate ligand, meaning it can bind at 2 regions of other atoms i.e. at the sulfur or the oxygen site. PVDF binds to DMSO at the oxygen site. Complex narrow absorbance peaks are represented in this range due to the overlapping curves of DMSO and PVDF material.

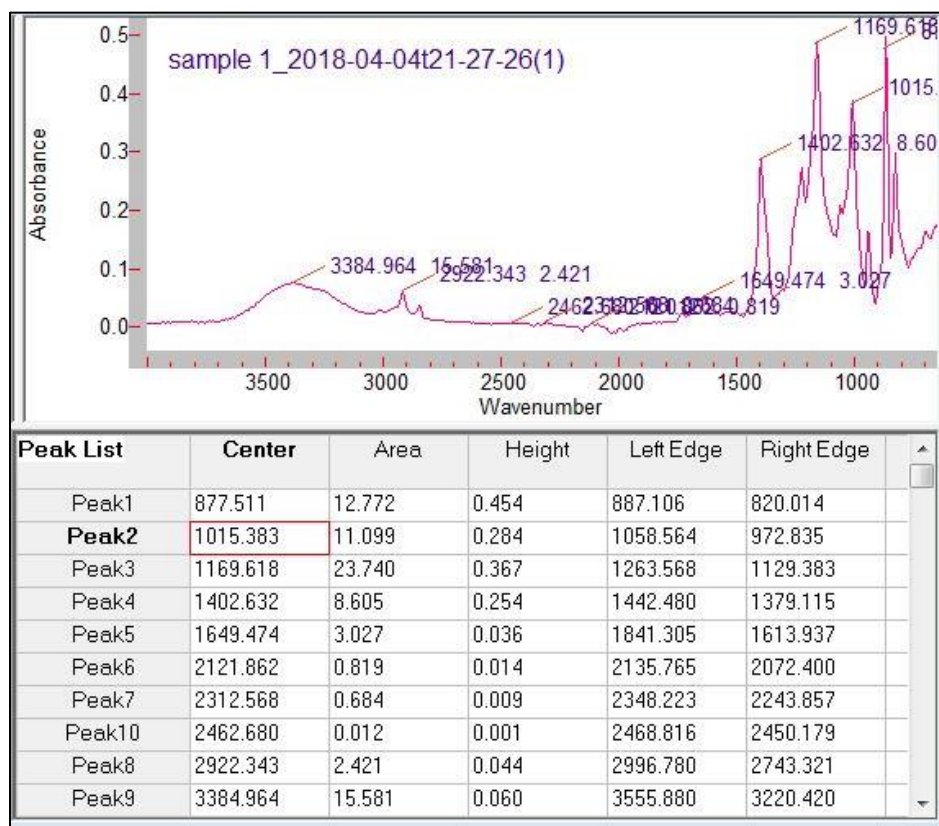


Figure 36. FTIR absorbance plot for PVDF/PZT 0-3 composite.

The region below the graph represents the Peak absorbance amplitude of the composite in a decreasing value of peak height where Peak 1 shows the maximum peak amplitude of PVDF absorbed at a wavelength of 877.5 cm^{-1} .

The curve shown indicates the presence of a wide peak of low intensity in the range of $3100\text{-}4000 \text{ cm}^{-1}$ which did not exist in the FTIR result of the individual material. This wide peak with peak depicts the O-H bond due to carboxylic acid present in PVDF. PVDF is also absorbed in the range of $2750\text{-}3200 \text{ cm}^{-1}$ with a peak at 2922.343 cm^{-1} indicating the presence of asymmetric stretching vibration in the C-H bond present in vinylidene $\text{CH}_2=$ and indicates the absorption of CH_3 in the carboxylic acid.

PZT, on the other hand, is shown to absorb at in a wavelength range of $2750\text{-}3200 \text{ cm}^{-1}$ and in the range of $500\text{-}900 \text{ cm}^{-1}$. Addition of PZT is said to enhance the β -phase PVDF.

Performance test for the comparison between α and β phases of PVDF have not been performed. With reference to the document written by S. Satapathy¹ and team ‘Crystallization [76] of PVDF with DMSO, and that the composite has been annealed at a temperature of ~80-100 °C for a span of 4-5 hours, the graph should predominantly indicate a major β -phase of PVDF as a conversion from its α -phase and is absorbed at a wavelength of 1275 cm^{-1} [77].

3.2.1.2. X-Ray diffraction

The XRD plot shows the dispersion of 4 different materials in the substrate sample which includes Lead Titanium Zirconium Oxide, Polyvinylidene fluoride, Gold and Lead Zirconium Oxide. It is observed that Lead Titanium Zirconium Oxide or PZT have higher intensity compared to the others owing to its highly crystalline nature. The presence of Lead Zirconium Oxide is also seen in the XRD-plot in Figure 37, which can be interpreted that PZT materials have been dispersed into its component oxides due to hot-pressing at high temperature and pressure.

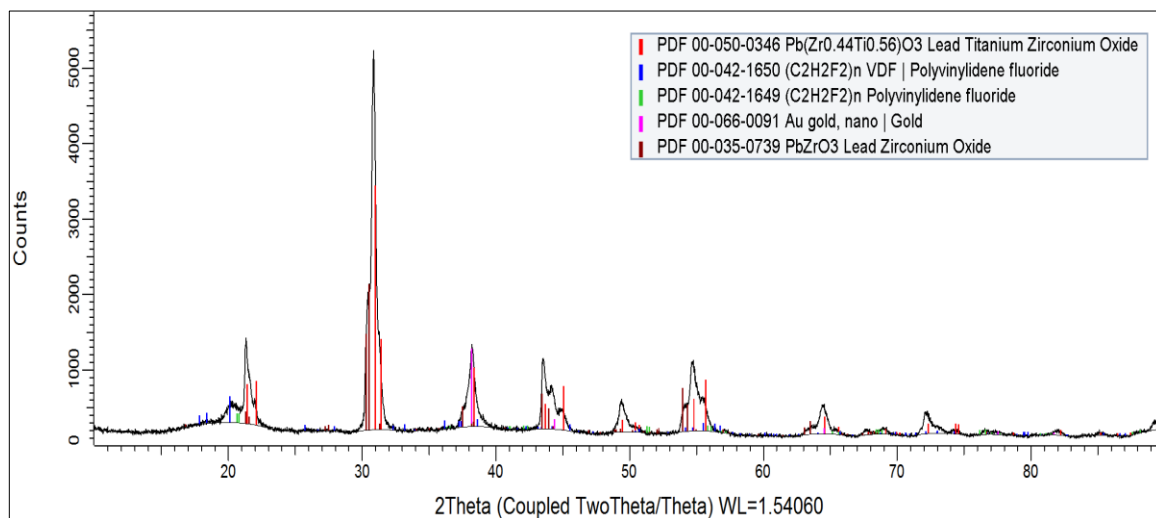


Figure 37. XRD plot representing the chemical composition in the obtained composite.

The intensity of XRD plots shows varying peaks depending upon the size of the crystallite, its orientation and the texture. Hence the XRD peak is expressed in arbitrary units.

PZT is shown to have the highest peak of ~5400 counts showing its high crystalline nature. When compared to PZT, PVDF, indicated by blue lines, is shown to have a very low peak intensity of 0-700 counts representing its semi-crystalline nature [78].

3.2.2. Piezoelectric Testing of the Composite Substrate

Once the sample was polarized, the density of the PVDF-PZT composite was measured by weighing the material using a digital balance. It was seen that for a volume of $3.2 \times 10^{-6} \text{m}^3$, the mass of the sample was $9.1 \times 10^{-3} \text{kg}$ and hence the density was found to be 2843kg/m^3 .

The piezoelectric strain coefficient is measured using YE2730A d33 piezometer which as shown in Figure 37 which shows a reading of ~22pC/N (or 22pm/V) at 250mN of force. Also, the dielectric constant ϵ_r was used for the available numerical resource and has a value of 18.09.



Figure 38. d33 measurement of the polarized sample.



Figure 39. Device used to set mN force to the sample.

With the values of d_{33} and ϵ_r calculated, the piezoelectric strain coefficient g_{33} is calculated from the following relation:

$$g_{33} = \frac{d_{33}}{\epsilon_0 \epsilon_r}$$

where ϵ_0 is the permittivity of free space (8.85×10^{-12} F/m). The value of g_{33} was calculated to be 0.137 V/m.

3.2.3. Testing of the SAW Device

SAW wireless sensing has reduced the computational time of signal processing calculations by a tremendous amount. A single centralized data acquisition system is used to measure and analyze a network of distributed sensors. It reduces the need for computing individual waveform of the signal generated for its frequency shifts, time delays, and impedance matching.

4. Results and Discussions

4.1. Results in Substrate Fabrication

4.1.1. Light Microscopic Image

Figure 40 shows the various compositions of PVDF/PZT in a substrate and the image was observed under a light microscope of 60x magnification.

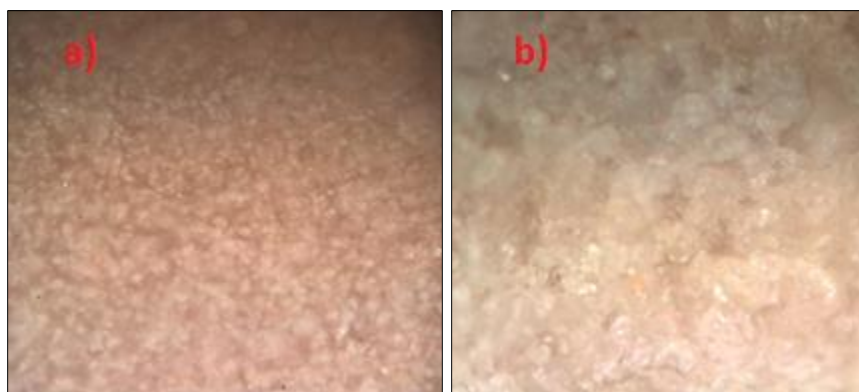


Figure 40. Microscopic image of the substrate a) Top-view, b) Bottom-view.

The top surface of the fabricated sample consisted of a finer and smoother nature compared to the bottom which was coarse and rough. The variation of coarseness was due to the settling down of dense PZT powder at the bottom of the petri dish during solvent evaporation phase which occurred at the time of substrate fabrication.

4.1.2. Scanning Electron Microscopic (SEM) Image

The surface of the substrate was visualized under SEM. It was noticed that during the initial trials the PZT particles in PVDF were improperly bonded due to the insufficient mixing of PZT powders in the PVDF matrix. Some of the powders remained as tiny coagulated mass, which when visualized under the SEM showed a granular size of 20-30 μ m.

Table 3. Chemical composition of the composite.

Properties	Values
DMSO	15ml
PVDF	3.8g
PZT content	50 vol.% of PVDF-DMSO solution
The average granular size	3 μ m - 30 μ m.

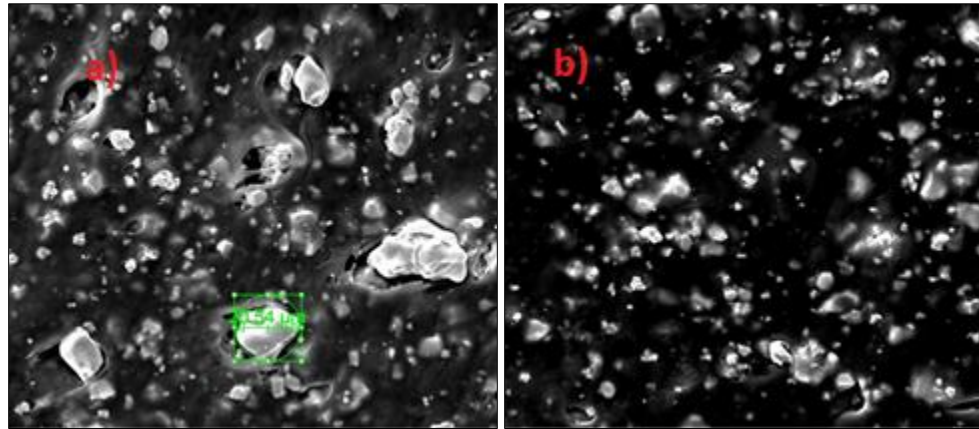


Figure 41. SEM images with a) Non-uniform particle distribution in PVDF matrix
b) Uniform particle distribution in PVDF matrix.

With this in concern, the PZT powder was subjected to rigorous stirring for about 12hrs. It was then sputtered with a micro layer of gold and visualized under SEM for better conduction as shown in Figure 41. It then showed an average granular size of 3-10 μ m.

A Comparison was performed with the research done by T.Siponkoski and his team to match the visualization [79] of 50% PZT content in PVDF shown in Figure 42. It was noticed that the SEM image of the obtained composite matched well with 50% PZT content which shows equal volume fraction of PVDF and PZT. Note that the sputtered gold created a blackish region on the image.

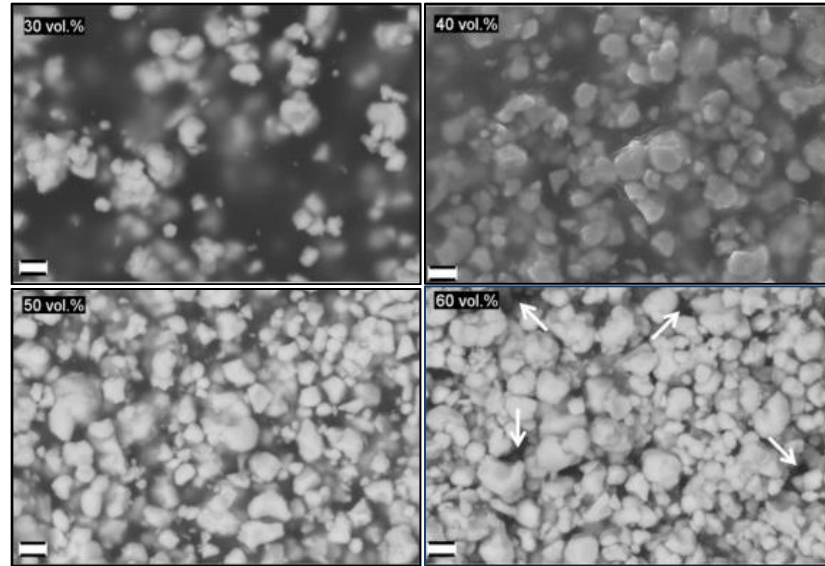


Figure 42. SEM images used for comparison of volume fraction [79].

4.1.3. Comparative Study of PVDF-TrFE/PZT and PVDF/PZT Composites:

During the experiment, it was noticed that the flexibility of PVDF/PZT sample gradually reduced during the transition of PZT content from 40-50% whereas, in case of PVDF-TrFE/PZT sample, the sample remained far more flexible even at 50% PZT content. It could be interpreted that even though 50% PZT content in PVDF maintained the flexibility, the overall sample would show a low fatigue life than PVDF-Trifle/PZT, even though the fatigue test was not performed. PVDF/PZT had a brittle nature to its flexibility and the sample had the tendency to rupture when subjected to buckling along the surface. On the other hand, it was easier to work with PVDF-TrFE/PZT composite because it could be easily folded/buckled several times and still wouldn't rupture easily.

It was also noticed that during photolithography PVDF/PZT sample absorbed most of the photoresist which was spin coated on the surface due to the surface coarseness and made the sample surface look maroon, the color of the photoresist, which was hard to be developed

away, and in turn the etchant couldn't etch away the deposited gold layer easily. On the other hand, the photoresist on the PVDF-TrFE/PZT surface was removed easily using the developer and the etchant clearly etched away from the deposited gold layer unexposed to UV radiations.

4.2. Photomask Design and Development

For the design of photomask, it was required to provide the necessary IDT dimensions. The parameters used in designing the IDT for a 50:50 PVDF-TrFE/PZT substrate is shown in the table below. The IDT finger width was designed to 9.1 microns initially and the parameters were calculated as shown.

Table 4. SAW device parameters [80].

Parameters	Symbol	Value	Units
Wavelength	λ_0	72.8	μm
Wave velocity	v	2600	m/s
Piezoelectric coupling coefficient	k_2	.0014	
Center frequency	f_0	35	MHz
Delay line length	L	3.6	mm
Characteristic Impedance	R_g	50	Ω
No. of finger pairs	N_{p1}	12	
No. of finger pairs	N_{p2}	6	
Aperture	W_t	5.1	mm
Finger spacing	W_f	9.1	μm
Finger width	E_w	9.1	μm
Bus bar height	BBH	36	μm

With these parameters, double-electrode type IDTs were designed on a free version of Layout Editor Software. The busbars were designed to maintain the input port at 0.9 mm distance from each other to accommodate for testing as shown below in Figure 43:

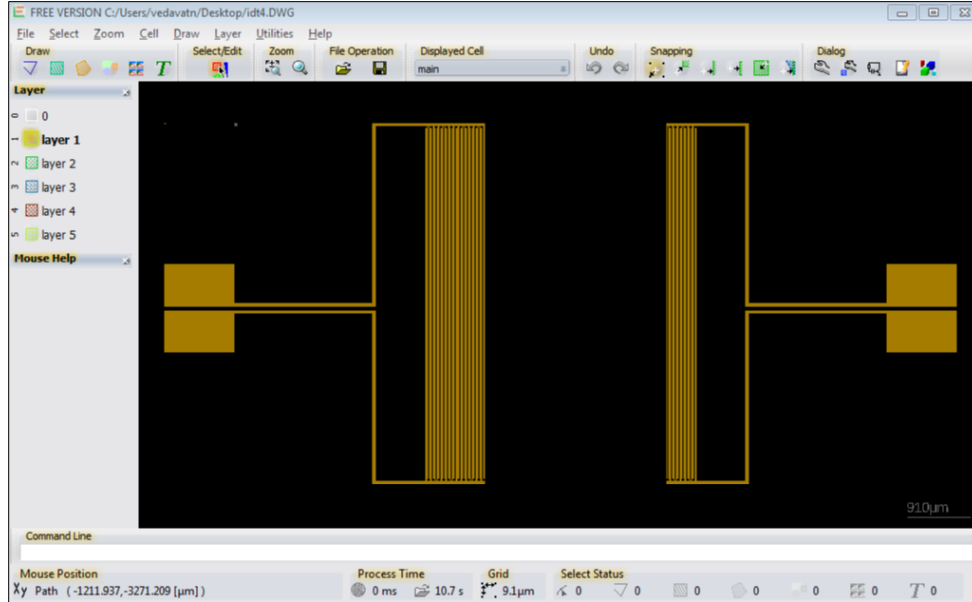


Figure 43. IDT design sketched on Layout Editor.

The fingers and the finger gap were designed with $9.1\mu\text{m}$, which almost blurred the electrodes together. Also, during photolithography, the electrodes could easily be etched away and the equipment in the laboratory were limited to maintain such dimensional precision. To eliminate this problem, the thickness of the electrodes was increased. The electrode thickness was hence set to 100 microns by reducing the frequency of the acoustic wave. Table 5 and Figure 44 represents the modified IDT dimensions to compensate for the drawbacks.

Table 5. Modified IDT dimensions.

Parameters	Symbol	Value	Units
No. of finger pairs	N_{p1}	6	
No. of finger pairs	N_{p2}	3	
Aperture	W_t	5.1	mm
Finger spacing	W_f	100	μm
Finger width	E_w	100	μm
Bus bar height	BBH	250	μm

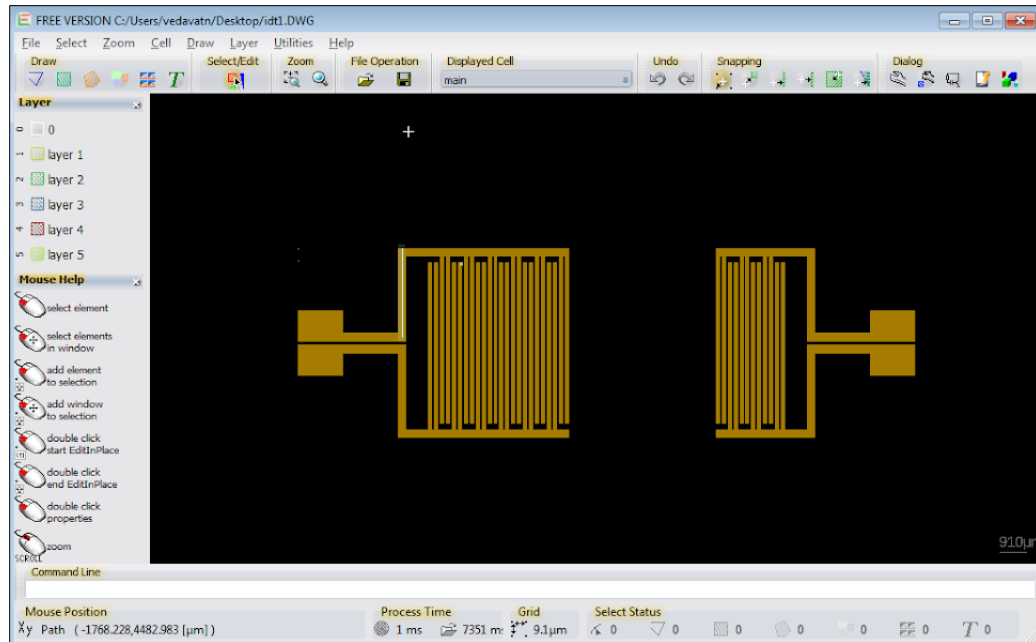


Figure 44. Modified IDT design sketched on Layout Editor.

The design was then patterned on AutoCAD with two different IDT thickness configurations as shown in Figure 45.

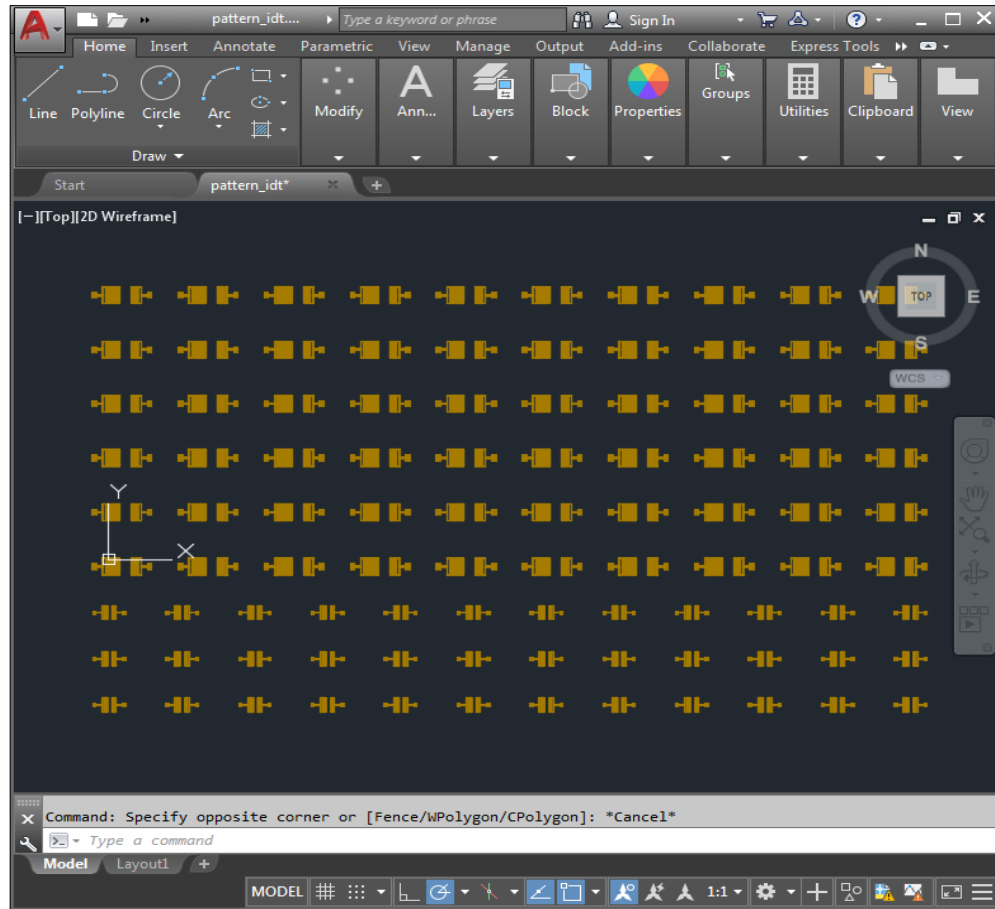


Figure 45. Modified IDT design sketched on Layout Editor.

The upper three-quarter of the pattern was designed with an electrode width of 100 microns with necessary variations in the height and bus bar width, and the lower patterns were designed with an electrode width of 9 microns as a support design during testing as shown in Figure 45. Patterning was done to develop the photomask. To generate a positive photomask, the designed pattern was sent to Artnet Pro Inc, CA. The generated design was printed in a black and white format which was then used during photolithography.

IDTs printed on the substrate material is shown in Figure 46. a), which shows the fine lines of electrodes. Some parts of the substrate were not etched properly due to insufficient UV radiations reaching the photoresist coated surface, and that happened due to surface

deformations. Figure 46. b) shows the IDT fingers visualized under a 60x resolution microscope.

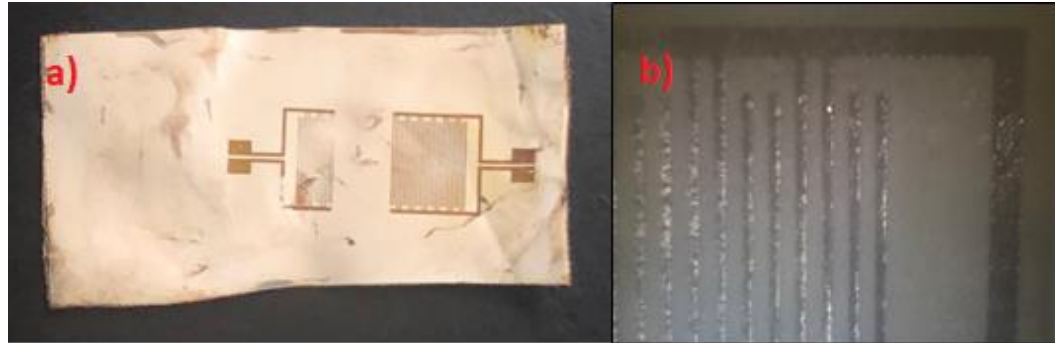


Figure 46. a) IDTs developed using photolithographic process, b) IDT fingers visualized under a microscope.

4.3. SAW Responses Using MATLAB

SAW device calculation was performed on MATLAB with codes extracted from previous ERAU thesis (done by Johannes Osse, 2017) and the plots were obtained for the modified IDT dimensions.

For the first order impulse response method, the graph of frequency response was obtained by the fast fourier transform of the raw signal. The graph represents a center frequency of 3.25 MHz. The Center frequency is defined as the frequency at which the impedance match between the RF signal and the input IDT of the SAW device occurs for maximum signal transduction. Generally, a higher value of center frequency is necessary for better sensitivity which reduces the size of the SAW device. Since fabrication of such tiny IDT finger width is quite a challenge, the SAW center frequency was reduced to a lower value and the IDT finger width was increased to compensate the reduction in frequency and thus maintain the acoustic wavelength.

The figure represents the insertion loss occurring in the SAW device, which is the loss generated during the installation of IDT on the substrate surface. The insertion loss is seen to be minimum at the center frequency of the SAW device. It is of the order of 25dB representing a low loss. Experimental values of insertion loss could be much higher.

SAW device admittance is the sum or superposition of the conductance and susceptance, defined as the ratio of the input current to voltage. It is represented in Figure 46 which shows that the admittance is maximum at the center frequency represented by a sharp peak of low bandwidth.

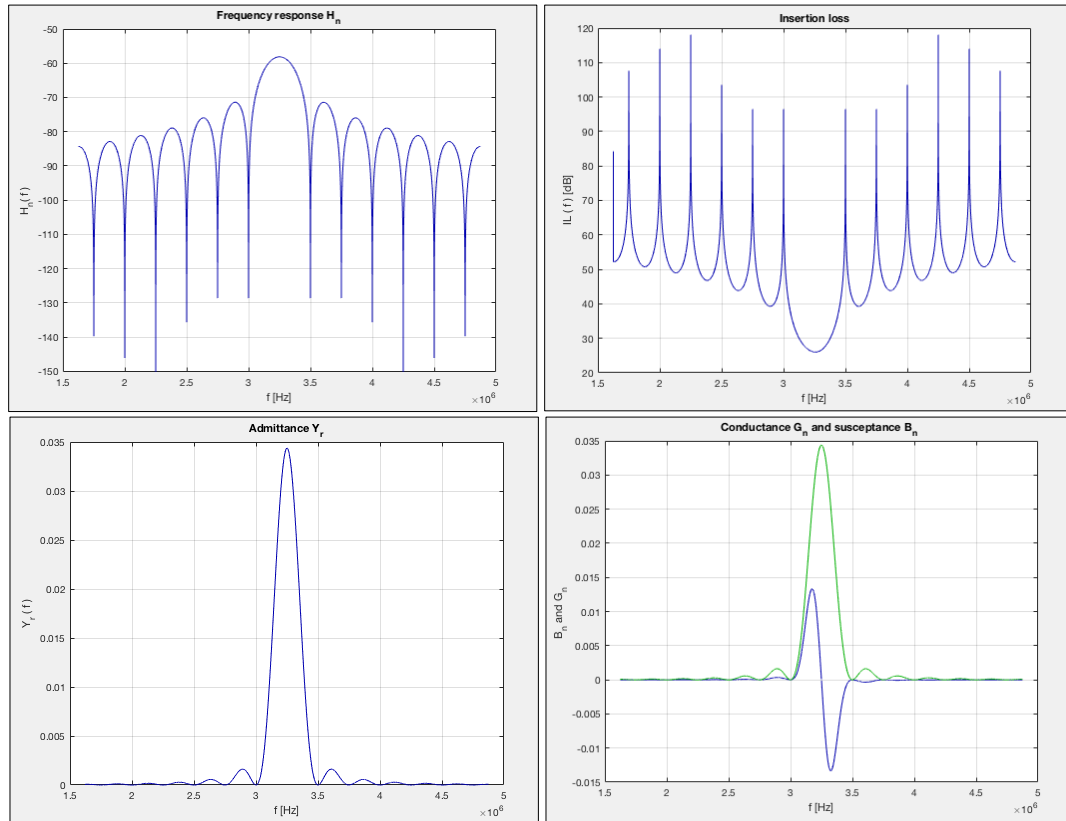


Figure 47. Shows the frequency response, insertion loss, admittance, conductance, and susceptance obtained from the first order impulse response model [80].

Figure 48 shows the Frequency response obtained from the cross field or transmission matrix approach. The ripples in the graph depict the loss due to triple transit reflection between the transducers. This expresses that the cross-field method considers the losses during SAW operation. To keep the losses at a minimum, the impedance of the source signal must match with the impedance of the input IDT. The green curve shows the phase plot overlapped on the frequency curve.

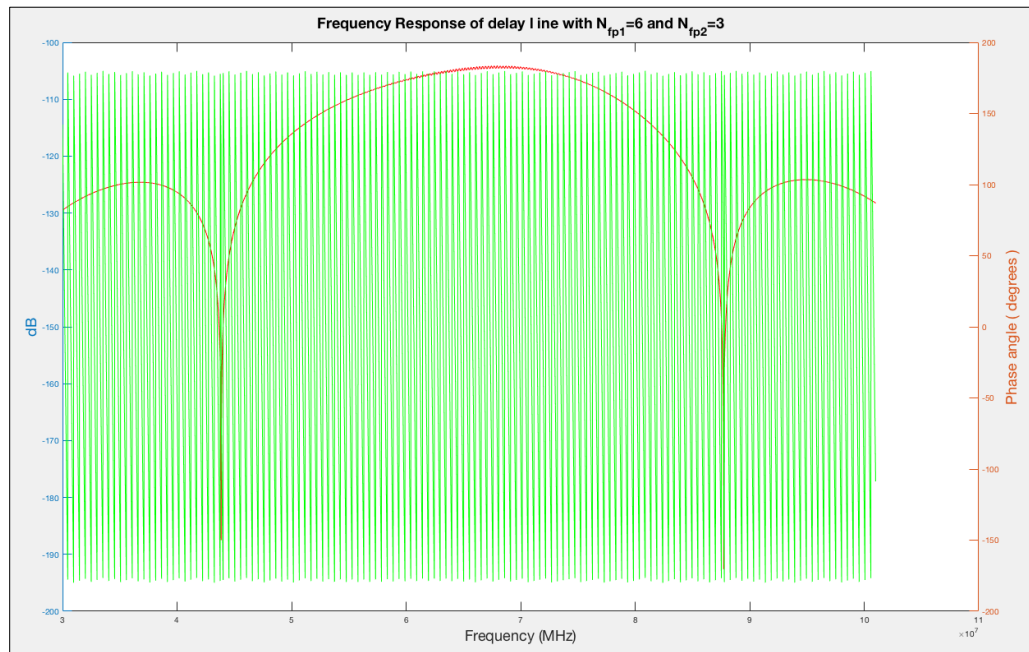


Figure 48. Represents the frequency response of the second order cross-field model.

4.4. Testing of the SAW Device

SAW wireless sensing has reduced the computational time of signal processing calculations by a tremendous amount. A single centralized data acquisition system is used to measure and analyze a network of distributed sensors. It reduces the need for computing individual waveform of the signal generated for its frequency shifts, time delays, and impedance matching.

Radio Frequency(RF) testing on the SAW device was performed by connecting 2 RF probes to the input and output IDTs which in turn was connected to a KEYSIGHT E5071C ENA series Network Analyzer. An RF beam of 10dBm was provided to the IDT input and the frequency was varied from 9 kHz to 8.5 GHz. Figure 49 a) and b) show the probes connected to the input and output terminals of the IDT and the setup visualized under the microscope of 10x resolution.

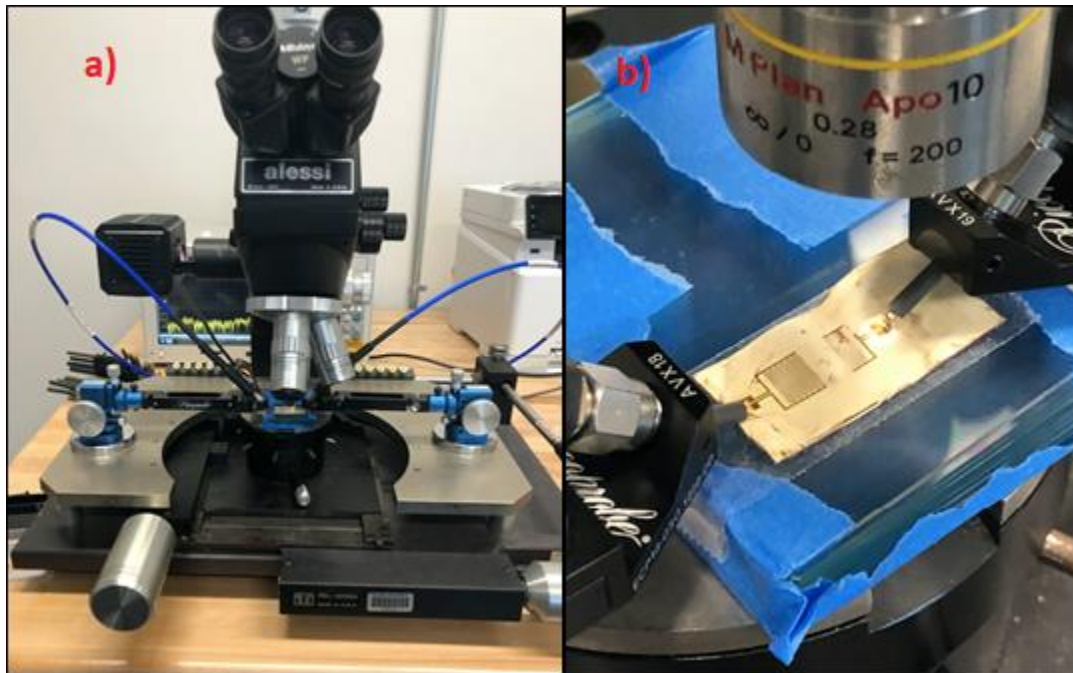


Figure 49. a) and b) Sensor attached to Network Analyzer through the RF probes.

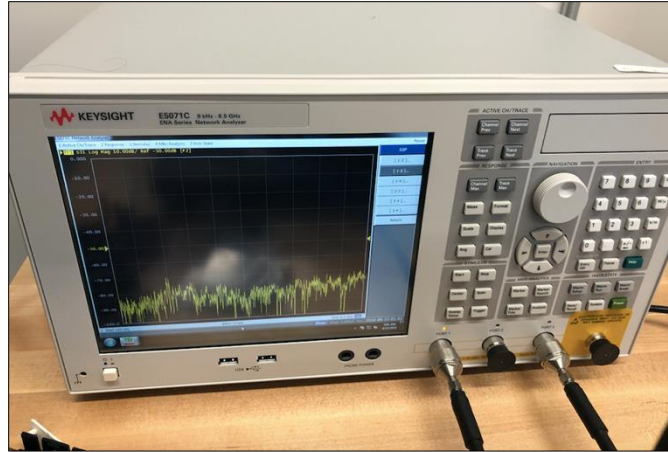


Figure 50. SAW transmission signal displayed on Network Analyzer.

Figure 50 shows the network analyzer displaying the transmission plot for amplitude change of the SAW delay line sensor when only the input IDT is connected to the RF probe.

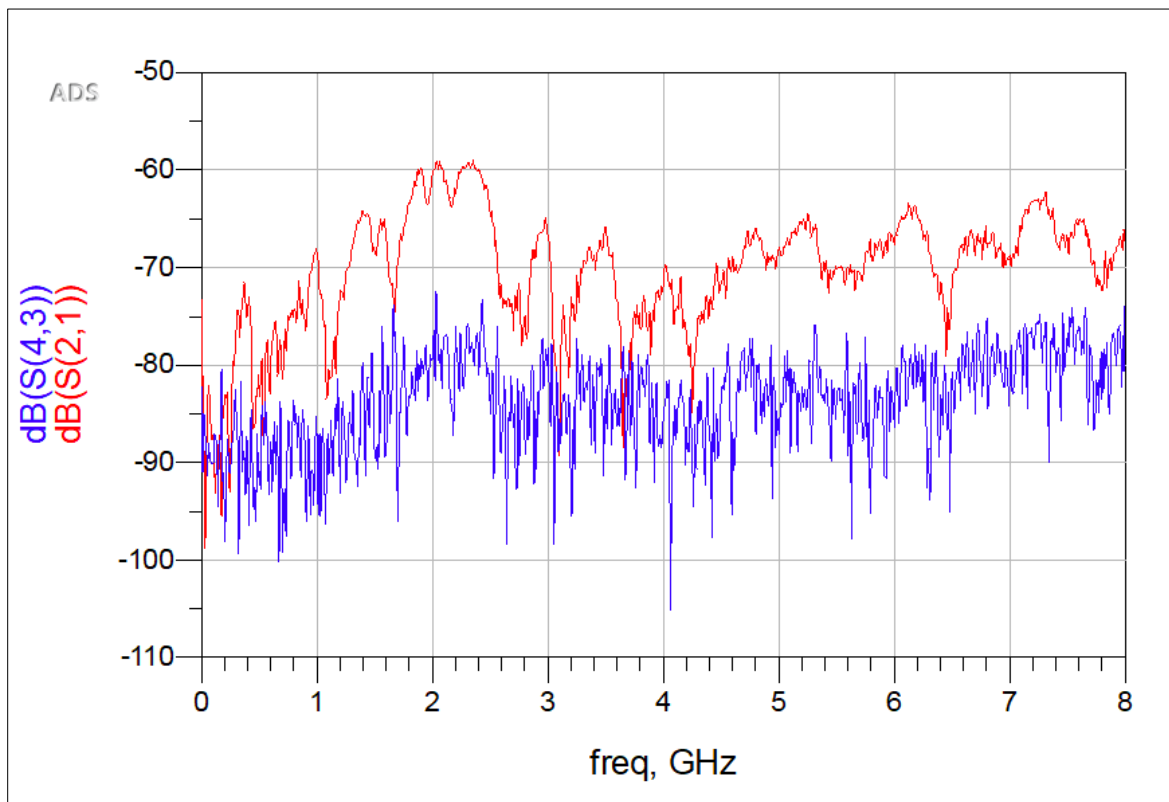


Figure 51. SAW transmission curve.

SAW signal transmission is presented in Figure 51. Variation of the S21 parameter for the sensor with the RF probes connected both to the input and the output IDTs is shown by the red curve and the frequency variation with S-parameter for the probe connected only to the input IDT is represented by the blue curve.

The maximum response peak occurs for the sensor is seen to occur at 2.1GHz. Since the range of frequency is displayed from 0-8GHz, smaller scale frequency response could not be interpreted much. The insertion loss of 60dB shows a low signal level at the output. This insertion loss caused in the device causes a large variation in signal response at the output due to noise. The signal bandwidth can be visualized to be ~3-4MHz with close interpretation. The curve in the transmission has irregular variation due to lack of impedance matching. While the impedance of the RF signal is 50Ω , the impedance of the sensor depends on the IDT geometry, resonance frequency, wave attenuation and delay line [81]. An ideal IDT that matches an exact value of impedance is difficult to be designed and requires precise tools for fabrication. Also, the ripples in the plot are observed to be caused due to various losses such as the improper impedance matching, triple transit interference, effect of metallization of IDT and electromagnetic resonance of the IDT on the substrate.

Figure 52 represents the phase change of SAW signal with respect to the frequency.

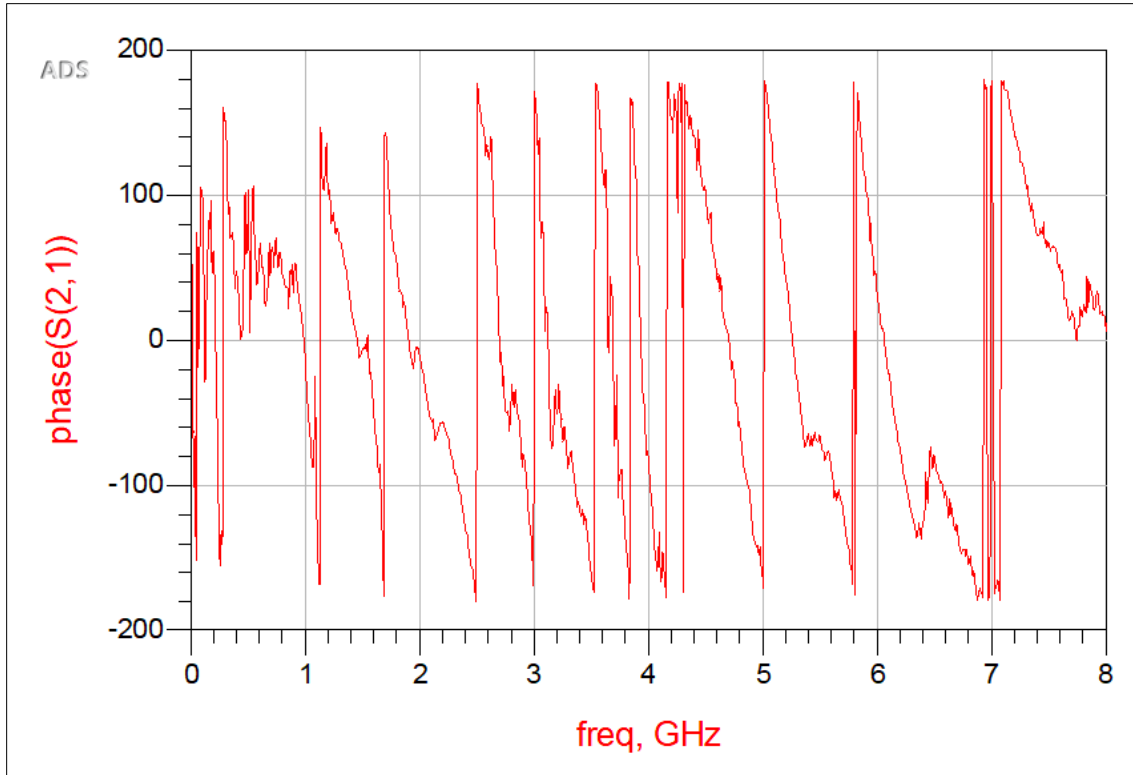


Figure 52. SAW phase curve.

Phase v.s. frequency plot gives the degree to which the pair of frequency components of waves transmitting from the input to the output IDTs are out of phase. Here the range is in between 180° to -180° . When the phase change of the device is measured with that obtained by strain measurements in the device, the shift in the phase curve could help us interpret the strain undergone by the sensor. The phase plot is seen to have irregular slanted lines due to the reflection from the edges and the triple transit interference during wave propagation. With minimal losses in the device, most of the lines on the phase plot would stand vertical and compact without much anomalies.

When the external parameters are sensed by the device in the delay line region, the velocity of the wave propagating in the delay line is strongly affected. If the sensor is subjected to tension, compression and bending, or even to a higher temperature, the length and elasticity

constants of the substrate is changed. These changes in dimension and properties cause changes in velocity and phase in the delay region, which then proportionally shift the center and resonant frequencies with time delay and wave attenuation between the IDTs.

5. Conclusion

The study deals with the fabrication of a piezoelectric sensor made flexible using PZT/PVDF and PZT/PVDF-TrFE composite as the substrate with deposition of gold IDTs on the surface in a delay line configuration, enabling the device to transmit waves and detect strain at the delay line region of the SAW sensor.

The analytical study of fabrication of PZT/PVDF substrate is performed by a series of fabrication stages by dissolving PVDF and PVDF-TrFE in DMSO solvent, mixing PZT powder onto it and hot pressing the obtained mold. The film thus obtained is polarized to impart piezoelectric properties to the PZT/PVDF and PZT/PVDF-TrFE composite. Addition of PZT in powder is shown to have improved the piezoelectric response and stabilized electromechanical coupling coefficient and the dielectric values. Sample polarization is conducted, and the sample was visualized and tested using FTIR scanning, X-Ray diffraction, and SEM microscopy.

Due to the superior permittivity of β phase PVDF, it could be electrically polarized by mechanically stretching and poling it at a high electric field. The net dipole moment attained facilitated PVDF and its copolymer film to achieve its piezoelectric properties. Electrical polarization also caused PVDF/PVDF-TrFE to accumulate large electric fields, enabling them to possess piezoelectric properties. PVDF or its copolymer was proved to be one of the best materials considered to attain flexibility which processes other advantages such as low cost, low density, eminent pliability, low electrical and mechanical impedance, efficient response time, low power consumption, biocompatibility, and non-toxicity.

During the substrate fabrication uniform distribution of the ceramic powder was one of the necessities. Uneven distribution of the ceramic in the solution could lead to the formation of thickened mass within the solution which can result in a variation of piezoelectric properties in the cast at each point. A solution to prevent the coagulated masses of the ceramic in the solution was by ultrasonic heating of the mixture which reduces the polymer viscosity. Poor mixing could also result in improper adhesion between the ceramic and the polymer and could even create air bubbles in the cast.

Once the substrate was polarized, the IDTs were made to incorporate on its surface to achieve the electromechanical wave conversion on the surface of the sensor and thus detect the frequency response of the system. Design of IDT was a challenging task which required high accuracy procedures such as photolithography to obtain finger thickness as low as 100nm. The necessary photomask was designed to be used during photolithography and the process was conducted with care, precision and in an enclosed room with no lights. The process of etching was also a challenging task and required a specific amount of time, which if crossed could etch away the fine electrodes and reduce its thickness, or even erase the entire electrode.

D33 meter showed a fluctuation between 19-23pN/mm. Due to the problems in arcing and limited material and time available, the polarization process was performed at 12kV/mm for 3 hours instead of 20kV/mm for 1 hour. It has not been confirmed that the prolonged exposure could be a means to tackle the polarization process, but since it gave a similar result assumption was made that the polarization process was complete.

RF testing of the sample was performed by sending and receiving RF waves from the RF probes connected to the sensor which could interpret the S-parameters and the

frequency response of the sample. The sample if tested for strain could provide the transmission and reflection characteristics of the sensor during strain measurement and thus the shift in the amplitude and phase of the graph could provide information on the strain.

SAW sensors can thus compile sophisticated signal processing functions into a single unit. Several hundreds of capacitances and inductors can, therefore, be gathered into a single tiny chip. Also due to their mass production capability and inexpensive photolithography technique, the expense of each sensor reduces drastically. The passive wireless SAW sensor thus generated is used in filter oscillators, actuators, resonators, chemical and bio-sensing and even in the tires of Automobiles or airplanes. Due to their passive nature, they can also be monitored in any harsh environment.

6. Future Work

This project has been presented for the development of a SAW sensor capable of sensing strain. Even though the device has been fabricated, there are several further discrepancies to be resolved. The SAW device modelling has not been performed on the piezoelectric substrate with the exact data interpreted from its result. The velocity of the SAW substrate has been assumed from a previous research written by Johannes, an Embry Riddle Alumni, and its frequency response plot have been determined with the procedures followed from his MATLAB files. The device velocity of propagation and the dielectric properties will have to be tested with relevant equipment to perform these procedures. The dielectric constant of the material could not be tested and was again assumed from a previous research and with this, the g_{33} parameter was calculated.

The XRD and FTIR plots are obtained only for the PVDF/PZT composite and not for the PVDF-TrFE/PZT sample since the usage of PVDF-TrFE was decided only in the later stages of the experiment.. The device must be tested with the RF signal and the S-parameters need to be determined which provides the transmission and reflective characteristics of the SAW device. The device could then be tested on a structure for determining the strain.

7. Recommendation

The designed SAW device can be modified at various stages and tested for better accuracy and precision. The amount of PZT in the substrate can be varied and an optimum value of the PZT content could be determined to achieve the best result. A detailed study can be performed by comparing the PZT/PVDF composite with PZT/PVDF-TrFE composite and the advantage of using one over the other can be noted and made use of. Also, SAW substrate can be tested for durability by conducting fatigue, tensile, torsional testing along with the test for bucking and failure analysis.

The IDTs on the substrate can be modified by decreasing the thickness helping the device to reduce its acoustic wavelength and in turn increases the required RF signal and helps in better transmission characteristics of the device. The delay line type configuration of the IDTs can also be replaced by a resonator with additional reflective gratings added to the device for better device sensing. The device can also be subjected to a detailed simulation on ANSYS Piezo and Acoustics, COMSOL, ONScale or PZFlex for a better understanding of the propagating electromagnetic wave and for validating the numerical results by determining the wave properties.

Methods to reduce the losses in the SAW device can be studied in detail and be implemented for improved accuracy in the frequency response. It could also be modified for temperature, gas and pressure sensing. The device may be tested on a static structure and then a dynamic structure and analyzed for its strain characteristics. A combination of such sensors can be used to analyze a full-scale dynamic model like on a structural component of an aircraft or automobile or even in difficult to reach areas.

8. References

- [1] Sensors. (2018). Available: <https://www.kellertechnology.com/blog/7-types-of-sensors-for-object-detection/>, *Keller Technology Corporation*.
- [2] Rocha-Gaso, M. I., March-Iborra, C., Montoya-Baides, A., & Arnau-Vives, A. (2009). Surface generated acoustic wave biosensors for the detection of pathogens: A review. *Sensors*, 9(7), 5740-5769.
- [3] Holloway, A. F., Nabok, A., Thompson, M., Ray, A. K., Crowther, D., & Siddiqi, J. (2003). New method of vapour discrimination using the thickness shear mode (TSM) resonator. *Sensors*, 3(6), 187-191.
- [4] Rayleigh, L. (1885). On waves propagated along the plane surface of an elastic solid. *Proceedings of the London Mathematical Society*, 1(1), 4-11.
- [5] White, R. M., & Voltmer, F. W. (1965). Direct piezoelectric coupling to surface elastic waves. *Applied physics letters*, 7(12), 314-316.
- [6] Williamson, R. C. (1977). Case studies of successful surface acoustic wave devices. *IEEE Ultrasonics Symposium*, 460-468.
- [7] Seifert, F., Bulst, W. E., & Ruppel, C. (1994). Mechanical sensors based on surface acoustic waves. *Sensors and Actuators A: Physical*, 44(3), 231-239.
- [8] Reeder, T. M., & Cullen, D. E. (1976). Surface-acoustic-wave pressure and temperature sensors. *Proceedings of the IEEE*, 64(5), 754-756.
- [9] Holland, M. G., & Claiborne, L. T. (1974). Practical surface acoustic wave devices. *Proceedings of the IEEE*, 62(5), 582-6.
- [10] Wolff, U., Dickert, F. L., Fischerauer, G. K., Greibl, W., & Ruppel, C. C. (2001). SAW sensors for harsh environments. *IEEE Sensors Journal*, 1(1), 4-13.
- [11] Scholl, G., Schmidt, F., Ostertag, T., Reindl, L., Scherr, H., & Wolff, U. (1998, May). Wireless passive SAW sensor systems for industrial and domestic applications. *Frequency Control Symposium, Proceedings of the IEEE*, 595-601.
- [12] Kalinin, V. (2004). Passive wireless strain and temperature sensors based on SAW devices. *IEEE Radio and Wireless Conference*, 187-190.
- [13] Chin, T. L., Zheng, P., Oppenheim, I. J., & Greve, D. W. (2010). Surface acoustic wave devices for wireless strain measurement. *Sensors and Smart Structures Technologies for Civil, Mechanical, and Aerospace Systems*, 764(7), 764-743.

- [14] Ye, X., Fang, L., Liang, B., Wang, Q., Wang, X., He, L., & Ko, W. H. (2011). Studies of a high-sensitive surface acoustic wave sensor for passive wireless blood pressure measurement. *Sensors and Actuators A: Physical*, 169(1), 74-82.
- [15] (2014). Piezoelectric Materials: Crystal Orientation and Poling Direction, *Comsol blog*.
- [16] Piezo Introduction. Available: <https://www.unictron.com/technology/piezo-introduction/>, *Unictron Technologies Corp*.
- [17] Sirohi, J., & Chopra, I. (2000). Fundamental understanding of piezoelectric strain sensors. *Journal of intelligent material systems and structures*, 11(4), 246-257.
- [18] Freitas, V. F., Santos, I. A., Botero, E., Fraygola, B. M., Garcia, D., & Eiras, J. A. (2011). Piezoelectric characterization of (0.6) BiFeO₃–(0.4) PbTiO₃ multiferroic ceramics. *Journal of the American Ceramic Society*, 94(3), 754-758.
- [19] Fujishima, S. (2000). The history of ceramic filters. *IEEE transactions on ultrasonics, ferroelectrics, and frequency control*, 47(1), 1-7.
- [20] Malik, A. F., Burhanudin, Z. A., Jeoti, V., Hashim, U., Foo, K. L., & Ismail, M. C. (2013). Acoustic wavelength effects on the propagation of SAW on piezo-crystal and polymer substrates. *Micro and Nanoelectronics (RSM), IEEE Regional Symposium*, 175-178.
- [21] Ögüt, E., Yördem, O. S., Menceloğlu, Y. Z., & Papila, M. (2007). Poly (vinylidene fluoride)/zinc oxide smart composite material. *Behavior and Mechanics of Multifunctional and Composite Materials*, 6526, 65260.
- [22] Akdogan, E. K., Allahverdi, M., & Safari, A. (2005). Piezoelectric composites for sensor and actuator applications. *IEEE transactions on ultrasonics, ferroelectrics, and frequency control*, 52(5), 746-775.
- [23] Zhou, A., Xie, Q., Yuan, Y., Zhang, Y., & Yao, S. (2000). Evaluation of electromechanical coupling factor for a piezoelectric quartz crystal in liquid phase. *Analytica chimica acta*, 419(2), 251-254.
- [24] Wang, Y., & Weng, G. J. (2015). Magnetoelectric coupling and overall properties of multiferroic composites with 0-0 and 1-1 connectivity. *Journal of Applied Physics*, 118(17), 174102.
- [25] Stroyan, J. J. (2004). Processing and characterization of PVDF, PVDF-TrFE, and PVDF-TrFE-PZT composites, *Thesis*.
- [26] Newnham, R. E., Skinner, D. P., & Cross, L. E. (1978). Connectivity and piezoelectric-pyroelectric composites. *Materials Research Bulletin*, 13(5), 525-536.

- [27] Akdogan, E. K., Allahverdi, M., & Safari, A. (2005). Piezoelectric composites for sensor and actuator applications. *IEEE transactions on ultrasonics, ferroelectrics, and frequency control*, 52(5), 746-775.
- [28] Osse, J. (2017). Development of a flexible saw sensor for strain sensing. *Embry-Riddle Aeronautical University Institution*.
- [29] Ruan, L., Yao, X., Chang, Y., Zhou, L., Qin, G., & Zhang, X. (2018). Properties and Applications of the β Phase Poly (vinylidene fluoride). *Polymers*, 10(3), 228.
- [30] Satapathy, S., Gupta, P. K., Pawar, S., & Varma, K. B. R. (2008). Crystallization of Beta-phase Poly (vinylidene fluoride) films using dimethyl sulfoxide (DMSO) solvent and at suitable annealing condition. arXiv:0808.0419.
- [31] Haghighashtiani, G., & Greminger, M. A. (2015). Fabrication, polarization, and characterization of PVDF matrix composites for integrated structural load sensing. *Smart Materials and Structures*, 24(4), 045038.
- [32] Mahale, B., Bodas, D., & Gangal, S. A. (2017). Study of β -phase development in spin-coated PVDF thick films. *Bulletin of Materials Science*, 40(3), 569-575.
- [33] Lima, J., Y., Kimb., S, Seo., Y. Enhancement of E-phase in PVDF by electrospinning. *Seoul National University*, 305-738.
- [34] Tancrell, R. H., Schulz, M. B., Barrett, H. H., Davis, L., & Holland, M. G. (1969). Dispersive delay lines using ultrasonic surface waves. *Proceedings of the IEEE*, 57(6), 1211-1213.
- [35] Campbell, C. (2012). Surface acoustic wave devices and their signal processing applications.
- [36] Tyagi, S., & Mahesh, V. G. (2012). Saw and interdigital transducers. *International Journal of Scientific & Engineering Research*, 3(12), 1-4.
- [37] IDT. Available: <http://www.electropedia.org/iev/iev.nsf/display?openform&ievref=561-01-41>. *International Electrotechnical Commission*, 561-01-41.
- [38] Anemogiannis, K. (1996). Surface wave interdigital transducer and surface wave filter with symmetric or predeterminable asymmetric transfer characteristic between input and output. *U.S. Patent*, 5,521,565.
- [39] SenGenuity. Available: http://www.sensorsportal.com/HTML/DIGEST/march_08/Temperature_sensor.htm. *Temperature Sensors*.
- [40] Malocha, D. C., Gallagher, M., Fisher, B., Humphries, J., Gallagher, D., & Kozlovski, N. (2013). A passive wireless multi-sensor SAW technology device and system perspectives. *Sensors*, 13(5), 5897-5922.

- [41] Hribšek, M. F., Tošić, D. V., & Radosavljević, M. R. (2010). Surface acoustic wave sensors in mechanical engineering. *FME transactions*, 38(1), 11-18.
- [42] Stoney, R., Donohoe, B., Geraghty, D., & O'Donnell, G. E. (2012). The development of surface acoustic wave sensors (SAWs) for process monitoring. *Procedia CIRP*, 1, 569-574.
- [43] Fall, D., Duquennoy, M., Ouaftouh, M., Smagin, N., Piwakowski, B., & Jenot, F. (2018). Optimization of interdigital transducers for the generation of surface acoustic waves over a large bandwidth (20–125 MHz). *Sensors and Actuators A: Physical*, 273, 303-310.
- [44] Kannan, T. (2006). Finite element analysis of surface acoustic wave resonators. *University of Saskatchewan, Doctoral dissertation*.
- [45] Fu, Y. Q., Luo, J. K., Nguyen, N. T., Walton, A. J., Flewitt, A. J., Zu, X. T., & Du, H. (2017). Advances in piezoelectric thin films for acoustic biosensors, acoustofluidics and lab-on-chip applications. *Progress in Materials Science*, 89, 31-91.
- [46] Mishra, D. (2015). Modeling of Interdigital Transducer Surface Acoustic Wave Device-Design and Simulation. *Communication Systems and Network Technologies (CSNT), Fifth International Conference*, 1327-1331.
- [47] Khaneja, M., & Mittal, U. (2008). Design and Modelling of a Two-port Surface Acoustic Wave Resonator using Coupling-of-modes Theory. *Defence Science Journal*, 58(3), 372.
- [48] Hartmann, C. S., Bell, D. T., & Rosenfeld, R. C. (1973). Impulse model design of acoustic surface-wave filters. *IEEE Transactions on Microwave Theory and Techniques*, 21(4), 162-175.
- [49] Elsherbini, M. M., Elkordy, M. F., & Gomaa, A. M. (2015). Analytical modeling and simulation of SAW filter using concave. *Indonesian Journal of Electrical Engineering and Computer Science*, 16(3), 495-501.
- [50] Hashimoto, K. Y., & Yamaguchi, H. (1996). General-purpose simulator for leaky surface acoustic wave devices based on coupling-of-modes theory. *Ultrasonics Symposium, Proceedings of the IEEE*, 57(3), 117-122.
- [51] Venkatesan, T., Banupriya, R., Pandiyarajan, G., & Haresh, M. P. (2015). Idealized P-Matrix based modelling and computational analysis of SAW delay lines for improved performance in sensors. *Journal of Environmental Nanotechnology*, 4(4), 56-61.
- [52] Khaneja, M., & Mittal, U. (2008). Design and modelling of a two-port surface acoustic wave resonator using coupling-of-modes theory. *Defence Science Journal*, 58(3), 372.

- [53] El Gowini, M. M., & Moussa, W. A. (2009). A reduced three dimensional model for SAW sensors using finite element analysis. *Sensors*, 9(12), 9945-9964.
- [54] Moten, S. (2010). Modeling of an ultrasonic transducer for cardiac imaging. Tech. Rep. D&C 2010.049, Dynamics and Control Group, Eindhoven University of Technology.
- [55] Jones, W. S., Hartmann, C. S., & Sturdivant, T. O. (1971). Modified equivalent circuit model for ultrasonic surface wave interdigital transducers. *Microwave Symposium Digest, IEEE GMTT International*, 58-59.
- [56] Wilson, W., & Atkinson, G. (2009). Comparison of transmission line methods for surface acoustic wave modeling, *NASA Langley research center*.
- [57] Campbell, C. (2012). Surface acoustic wave devices and their signal processing applications.
- [58] Ro, R., Tung, H. Y., & Wu, S. J. (2004). Design of two-track surface acoustic wave filters with width-controlled reflectors. *Japanese journal of applied physics*, 43(2R), 688.
- [59] Krishnamurthy, S. (2007). Wireless Passive Surface Acoustic Wave (SAW) Sensing System. *Western Michigan University, Doctoral dissertation*
- [60] Shen, L., Feng, S., Li, J., Chen, J., Li, F., Lin, H., & Yu, G. (2017). Surface modification of polyvinylidene fluoride (PVDF) membrane via radiation grafting: novel mechanisms underlying the interesting enhanced membrane performance. *Scientific Reports*, 7(1), 2721.
- [61] Ghaee, A., Sadatniab, B., Khosravic, M., Mansourpour, Z., & Ghadimid, A. (2017). Preparation and characterization of modified PVDF membrane induced by argon plasma with enhanced antifouling property. *Desalination and Water Treatment*, 64, 72-80.
- [62] Siponkoski, T., Nelo, M., Palosaari, J., Peräntie, J., Sobocinski, M., Juuti, J., & Jantunen, H. (2015). Electromechanical properties of PZT/P (VDF-TrFE) composite ink printed on a flexible organic substrate. *Composites Part B: Engineering*, 80, 217-222.
- [63] Liao, Y., Wang, R., Tian, M., Qiu, C., & Fane, A. G. (2013). Fabrication of polyvinylidene fluoride (PVDF) nanofiber membranes by electro-spinning for direct contact membrane distillation. *Journal of Membrane Science*, 425, 30-39.
- [64] Seema, A., Dayas, K. R., & Varghese, J. M. (2007). PVDF/PZT-5H composites prepared by hot press and tape casting techniques. *Journal of applied polymer science*, 106(1), 146-151.
- [65] DMSO. Available: <https://www.webmd.com/vitamins-and-supplements/dmsso-uses-and-risks#1>. *WebMD*.

- [66] Esterly, D. M. (2002). Manufacturing of poly (vinylidene fluoride) and evaluation of its mechanical properties. *Virginia Polytechnic Institute and State University, Thesis*.
- [67] Jain, A., Sharma, A. K., & Jain, A. (2015). Dielectric and piezoelectric properties of PVDF/PZT composites: A review. *Polymer Engineering & Science*, 55(7), 1589-1616.
- [68] Esterly, D. M. (2002). Manufacturing of Poly (vinylidene fluoride) and Evaluation of its Mechanical Properties. *Doctoral dissertation, Virginia Tech*.
- [69] Haghighashtiani, G., & Greminger, M. A. (2015). Fabrication, polarization, and characterization of PVDF matrix composites for integrated structural load sensing. *Smart Materials and Structures*, 24(4), 045038.
- [70] Vapor Deposition. Available: <https://www.sciencedirect.com/topics/earth-and-planetary-sciences/vapor-deposition>, *ScienceDirect*.
- [71] Film deposition process. Available: <https://www.memsnet.org/mems/processes/deposition.html>. *MEMSnet*.
- [72] Lithography. Available: <https://www.memsnet.org/mems/processes/lithography.html>. *MEMSnet*.
- [73] Infrared Spectroscopy. Available: http://www.chem.ucla.edu/~harding/notes/notes_14C_IR.pdf.
- [74] Bai, H., Wang, X., Zhou, Y., & Zhang, L. (2012). Preparation and characterization of poly (vinylidene fluoride) composite membranes blended with nano-crystalline cellulose. *Progress in Natural Science: Materials International*, 22(3), 250-257.
- [75] Benam, M. R. (2014). Monitoring the processing steps of PZT nano-powders by FTIR technique. *International Journal of Research and Reviews in Applied Sciences*, 18(2), 145.
- [76] Satapathy, S., Gupta, P. K., Pawar, S., & Varma, K. B. R. (2008). Crystallization of Beta-phase Poly (vinylidene fluoride) films using dimethyl sulfoxide (DMSO) solvent and at suitable annealing condition. arXiv:0808.0419.
- [77] Mandal, D., Henkel, K., & Schmeiber, D. (2012). The electroactive β -phase formation in poly (vinylidene fluoride) by gold nanoparticles doping. *Materials Letters*, 73, 123-125.
- [78] Zhang, P. Y., Xu, Z. L., Yang, H., Wei, Y. M., & Wu, W. Z. (2013). Fabrication and characterization of PVDF membranes via an in situ free radical polymerization method. *Chemical Engineering Science*, 97, 296-308.
- [79] Siponkoski, T., Nelo, M., Palosaari, J., Peräntie, J., Sobocinski, M., Juuti, J., & Jantunen, H. (2015). Electromechanical properties of PZT/P (VDF-TrFE) composite ink printed on a flexible organic substrate. *Composites Part B: Engineering*, 80, 217-222.

[80] Osse, J. (2017). Development of a flexible SAW sensor for Strain Sensing. *Embry Riddle Aeronautical University, Thesis*.

[81] Oh, H., Wang, W., Lee, K., Park, I., & Yang, S. Sensitivity improvement of wireless pressure sensor by incorporating a saw reflective delay line. *Division of Electronics Engineering Ajou University*, 443-749.

9. Appendix

A. IDT calculations for mathematical calculations

Inputs:

Material: PVDF-PZT composite

NBW=1.5 MHz

Bus bar height= $36 \times 10^{-6} m$

Assumptions:

Wave velocity, $v = 2600 m/s$

Characteristic Impedance, $R=50\Omega$

Capacitor/finger/m= $0.5 \times 10^{-12} pF/cm$

No. of finger pairs in input IDT=6

No. of finger pairs in input IDT=3

Electrode width=Width of the gap between the electrodes

Calculations:

Thickness of the SAW substrate, $t= 0.728mm$

$$\text{Max SAW wavelength} = \frac{t}{10} = \frac{728 \times 10^{-6}}{10} = 72.8 \times 10^{-6} m$$

$$\text{Calculated center frequency} = f_0 = \frac{v}{\lambda} = \frac{2600}{0.0728} = 35.71 \times 10^6 Hz$$

$$\text{Fractional Bandwidth, } B = \frac{NBW}{f_0} = \frac{1.5 \times 10^6}{35.71 \times 10^6} = 0.042$$

$$\text{Width of electrode, } E_w = \frac{\lambda}{8} = \frac{72.8 \times 10^{-6}}{8} = 9.1 \times 10^{-6} m$$

Electrode length, $W = 70 * \lambda = 70 * 72.8 \times 10^{-6} = 5096 \times 10^{-6} m$

Delay line length= $L = 100 * \lambda = 50 * 72.8 \times 10^{-6} = 3640 \times 10^{-6} m$

B. MATLAB Simulation for First Order Response

```

clear all ;
clc ;

%inputs
f0=50e6; %Synchronous frequency [Hz]
v=2600; %velocity of substrate [m/ s]
k=sqrt (0.0014); %Piezoelectric coefficient
BBH=250e-6; %Bus bar height [m]
Rg=50; %El e c t r i c a l (Y_0 characteristic) impedance
[Ohm]
C_fp=0.5e-12; %Capacitance per finger pair
lambda0=v / (4* f0); %Wavelength ; for double finger
design ,finger width is lambda/4
delay =6.25; %Delay l i n e length in wavelengths
Ew=100e-6; lambda0=8*Ew;
f0=v/lambda0; fmin=0.5* f0; %minimum frequency [Hz]
fmax=1.5* f0; %maximum frequency [Hz]
df =(fmax-fmin) /10000; %frequency step size del ta f
NBW=0.5e6; %Null bandwidth
%Electrode width for double electrode design
N_fp=round((2/NBW) * f0); %Number of finger pairs
f=fmin: df: fmax; %frequency range
W=(1/Rg) * (1/ (f0 *2*C_fp*N_fp)) * real (1/ (4*
k^2*N_fp+1i * pi));
W=5100e-6;
Wf=225e-6; %Finger bus bar spacing; for double finger
design spacing i s lambda/8 "> v/8* f0
Wt=W+Wf; %Finger height
%Calculations
for i =1: size (f, 2)
    if f (i)==f0
        x=0;
    else
        x=N_fp* pi * ((f (i)-f0) / f0);
    end
    Ga=8*k^2*C_fp*W* f0 *N_fp^2*(sin (x) /x) ^2; %Radiation
conductance
    CT=N_fp*C_fp*W; %Total IDT capacitance
    Ba=Ga* (sin (2* x)-2*x) / (2* x.^2); %Acoustic
susceptance
    H=2*k* sqrt (C_fp* f0) *N_fp* (sin (x) /x) ; %Frequency
response

```

```

    Yr ( i )=min(Ga+sqrt(-1) * (2* pi * f *CT+Ba) )
; %Admittance
    Zr ( i ) =1/Yr ( i ) ; %Impedance
    Hn( i ) =20* log10 ( abs (H/1) ) ;
    IL ( i )=-10*log10 ( (2*Ga*Rg) / ( (1+Ga*Rg)^2+min(Rg*
(2* pi * f *CT+Ba) )^2) ) ;
    Gn( i )=Ga/1;
    Bn( i )=Ba/1;
    L=1/(2* pi * f0 ) ^2*CT; %Matching series inductor [ (
s^2/F)=H]
    W=(1/Rg) * (1/ (2* f0 *C_fp*N_fp) ) * ( ( 4 * k^2*N_fp)
/(4* k^2*N_fp)^2+pi^2) ; %Aperture optimization
    Q( i )=imag( Yr ( i ) ) / real ( Yr ( i ) ) ;
end
figure(1);
plot ( f ,Hn,'LineWidth',1,'color',[0/255 0/255 175/255])
xlim( [15e5 50e5 ] )%ylim( [4 5] )
grid on
title('Frequency response H_n')
xlabel('f [Hz]')
ylabel('H_n( f )')
figure(2);
plot(f,IL,'LineWidth',1,'color',[0/255 0/255 175/255])
xlim([15e5 50e5])
%ylim( [4 5] )
grid on
title('Insertion loss')
xlabel ('f [Hz]')
ylabel ('IL ( f ) [dB]')
figure (3) ;
plot(f,Gn,'LineWidth',1,'color',[0/255 0/255 175/255])
xlim( [15e5 50e5])
%ylim( [4 5] )
grid on
title('Radiation condutance G_n')
xlabel ('f [Hz]')
ylabel ('G_n( f )')
figure (4) ;
plot ( f ,Bn , 'LineWidth',1,'color',[0/255 0/255 175/255])
xlim( [15e5 50e5] )
%ylim( [4 5] )
grid on
title ( ' Acoustic Susceptance B_n ' )
xlabel ( ' f [Hz] ' )
ylabel ( 'B_n ' )
figure (5) ;

```

```

plot( f , Zr , 'LineWidth', 1 , 'color' , [0/255 0/255
175/255])
xlim( [15e5 50e5] )
%ylim( [4 5] )
grid on
title ( 'Impedance Z_r' )
xlabel ( 'f [Hz]' )
ylabel ( 'Z_r ( f )' )
figure (6) ;
plot ( f , Yr , 'LineWidth', 1 , 'color' , [0/255 0/255
175/255])
xlim( [15e5 50e5])
%ylim( [4 5] )
grid on
title( 'Admittance Y_r' )
xlabel ( ' f [Hz] ' )
ylabel ( 'Y_r ( f )' )
figure (7) ;
hAxes = gca ;
plot ( hAxes , f , Bn , 'LineWidth', 1 , 'color' , [0/255
0/255 175/255]) ;
hold ( hAxes , 'on' ) ;
plot ( hAxes , f , Gn, 'LineWidth' , 1 , 'color' , [0/255
177/255 0/255] ) ;
xlim( [15e5 50e5] )
%ylim( [4 5] )
grid on
title ( 'Conductance G_n and susceptance B_n ' )
xlabel ( 'f [Hz]' )
ylabel ( 'B_n and G_n ' )

```

C. MATLAB Simulation for Second Order Response

```

%Simulation of the frequency response of SAW delay line
sensor
clear all ;
clc ;
f0=50e6 ; %center frequency
v=2600; %SAW velocity on the free sections of PVDF°PZT
composite
v_m=2500; %SAW velocity on the metallized sections of
PVDF°PZT composite
lambda_0=v/f0; %SAW wavelength
N_pf1=6; %Number of fingers in the input IDT
N_pf2=3; %Number of fingers in the output IDT
BBH=250e-6; %Bus bar height
C_fp=0.5e-12; %Capacitance per finger pair per unit length
k=sqrt(0.0014) ; %Electromechanical coupling coefficient of
PVDF°PZT composite , describes the energy conversion
%efficiency and potential sensitivity in A_se better way
than
%the piezoelectric coefficients
df =0.125*lambda_0 ; %free section  $\lambda/8$ 
dm=0.125*lambda_0 ; %metallized section  $\lambda/8$ 
fm=v_m/lambda_0 ; %frequency of metallized section
W=5300e-6; %Acoustic aperture, factor=80 to
%minimize finger resistance
d=5000e-6; %Length of the delay line (transmission line)
Z=1/( f0 *C_fp*W*k ) ; %acoustic impedance for free sections
without fingers
Z_m=1/(fm*C_fp*W*k ) ; %acoustic impedance for the
metallized sections with fingers
k11=(0.016+(0.02*BBH/lambda_0) ) * (2* pi /lambda_0) ; %Self
coupling coefficient for PVDF°PZT composite
i =1;
for f =30e6:5000:101e6 %Frequency range
    lambda=v/ f ; %wavelength
    omega=2*pi * f ; %c i r c l e frequency
    %Computation of the ABCD matrix for a single finger
    theta_f =2*pi * f * df /v ; %acoustic angle in free
region
    theta_m=2*pi * f * dm/v_m; %acoustic angle in metallized
region
    %Computation of the free region between fingers
    Af=cos ( theta_f ) ;
    Bf=sqrt(-1) *Z* sin ( theta_f ) ;
    Cf=sqrt(-1) * sin ( theta_f ) /Z;

```

```

Df=cos ( theta_f ) ;
%Computation of the metallized regions under fingers
Am=cos ( theta_m ) ;
Bm=sqrt(-1) *Z_m* sin ( theta_m) ;
Cm=sqrt(-1) * sin ( theta_m) /Z_m;
Dm=cos(theta_m) ;
%Cascading matrix for a single finger to calculate 2x2
A finger matrix
Afinger =[Af Bf ; Cf Df ]*[Am Bm;Cm Dm]*[ Af Bf ; Cf Df
] ;
A_se=Afinger (1 ,1) ; %Single finger matrix value in
1. Row and 1. Column respectively Afinger_11
B_se=Afinger (1 ,2) ; %Afinger_12
C_se=Afinger (2 ,1) ; %Afinger_21
D_se=Afinger (2 ,2) ; %Afinger_22
theta_d=2*pi * f *d/v ; %delay path
theta_e=acos (A_se ) ;
Ze=B_se /( sqrt(-1) * sin ( theta_e ) ) ;
%2x2 transmission matrix for a single finger of the IDT
t11 =0.5* (2*A_se+(B_se/Z)+Z*C_se ) ;
t12 =0.5* (Z*C_se-(B_se/Z) ) ;
t13 =( ( sqrt (-1) ) * tan ( theta_e /2) * (Z^0.5) )
/(2*Ze) ) *(-A_se-1-(B_se/Z)) ;
t21=-t12 ;
t22=conj(t11) ;
t23=sqrt(-1) * tan ( theta_e /2) * (Z^0.5) *(1+A_se-
(B_se/Z) ) /(2*Ze) ;
t31=2* t13 ;
t32=-2*t23 ;
t33=sqrt(-1) *omega*C_fp*W*0.5+ sqrt(-1) *2* ( tan (
theta_e /2) /Ze)-sqrt(-1)...
* ( sin ( theta_e ) * ( tan ( theta_e /2) ^2) ) /Ze
;
%computing the 2x2 IDT matrix
t1 =[ t11 t12 ; t21 t22 ]^N_pf1 ; %2x2 scattering
matrix T_p^N_input (N finger pairs )
t3 =[ t11 t12 ; t21 t22 ]^N_pf2 ; %2x2 scattering
matrix T_p^N_output(N finger pairs )
t111=t1 (1 ,1) ;
t121=t1 (1 ,2) ;
t123=t3 (1 ,2) ;
t113=t3 (1 ,1) ;
t213=t3 (2 ,1) ;
t223=t3 (2 ,2) ;
t211=t1 (2 ,1) ;
t221=t1 (2 ,2) ;
Bp=[ t13 ; t23 ]+[ t11 t12 ; t21 t22 ]*[-t13;-t23 ] ;

```

```

Cp=[ t31 t32 ] * [ t11 t12 ; t21 t22 ]+[-t31 -t32 ] ;
t33p=2* t33 +[ t31 t32 ]*[-t13;-t23 ] ;
Tp=[ t11 t12 ; t21 t22 ]^2;
B_N0= [ 0 ; 0 ] ; %B_N
C_N0=[0 0 ] ; %C_N
B_Nout = [ 0 ; 0 ] ; %B_N_out
C_Nout=[0 0 ] ; %C_N_out
t333 =(N_pf2/2) * t33p ; %from t33N = N* t33p + formula
t331 =(N_pf1/2) * t33p ;
%computing t13, t23, t31, t32, t33 values for the whole
IDT
%Input IDT
for i1 =1:(N_pf1/2) %dynamic loop , set the index value
i1 to 1 , 2 , 3 . . . up to value of N_p1/2
    B_N0=B_N0+(Tp^( i1 -1) ) *Bp;
    C_N0=C_N0+Cp*Tp^( i1 -1) ;
    t331=t331 +( (N_pf1/2)-i1 ) *Cp*Tp^( i1 -1)
*Bp; %t33N, for N=1 it is t331
end
%Ref lector
for i2 =1: (N_pf2/2)
    B_Nout=B_Nout+(Tp^( i2 -1) ) *Bp;
    C_Nout=C_Nout+Cp*Tp^( i2 -1) ;
    t333=t333 +( (N_pf2/2)-i2 ) *Cp*Tp^( i2 -1) *Bp;
end
%Def ini t ion of elements t_ (line row port) of
transmission line to
%the according T°matrix value (line, row)
t131=B_N0(1 ,1) ;
t133=B_Nout (1 ,1) ;
t231=B_N0(2 ,1) ;
t233=B_Nout (2 ,1) ;
t311=C_N0(1 ,1) ;
t313=C_Nout (1 ,1) ;
t321=C_N0(1 ,2) ;
t323=C_Nout (1 ,2) ;
%ABCD matrix of delay path
Ad=cos(theta_d) ;
Bd=sqrt(-1) *Z* sin ( theta_d ) ;
Cd=sqrt(-1) * sin ( theta_d ) /Z;
Dd=cos ( theta_d ) ;
%Computation of transmission matrix for delay path
d11=0.5* (2*Ad+ (Bd/Z) +Z*Cd);
d12=0.5* (Z*Cd-(Bd/Z));
d21=-d12;
d22=0.5* (2*Ad- (Bd/Z) -Z*Cd);
d2=[d11 d12 ; d21 d22 ] ;

```



```

    %Used subs t i tutions
    sub1=t1 *d2* t3 ;
    sub2=t1 *d2 * [ t133 ; t233 ] ;
    sub3=[ t311 t321 ] *d2* t3 ;
    sub4=[ t311 t321 ] *d2 * [ t133 ; t233 ] ;
    %computing Y°parameter (admittance) for the SAW delay
line
    y11 (i)=t331-(sub3(1 ,1)*t131/sub1(1,1));
    y12 (i)=sub4(1,1)-(sub3(1,1)*sub2(1,1)/sub1(1,1));
    y21 (i)=-t313*t131/sub1(1,1);
    y22 (i)=t333-(t313*sub2(1,1)/sub1(1,1));
    %Computing frequency response S21 using the Y parameter
    s11(i) =((1-y11(i)) *(1+y22(i))+y12(i)*y21( i ) ) /(
(1+y11 ( i ) ) *(1+y22 ( i ) )...
        -y12 ( i ) *y21 ( i ) ) ;
    s12(i)=-2*y12 ( i ) /( (1+y11 ( i ) ) *(1+y22 ( i ) ) -
y12 ( i ) *y21 ( i ) ) ;
    s21(i)=-2*y21 ( i ) /( (1+y11 ( i ) ) *(1+y22 ( i ) ) -
y12 ( i ) *y21 ( i ) ) ;
    s22(i) =((1+y11 ( i ) ) *(1-y22 ( i ) )+y12 ( i ) *y21
( i ) ) /( (1+y11 ( i ) ) *(1+y22 ( i ) )...
        )-y12 ( i ) *y21 ( i ) ) ;
    %Computing Z parameter as impedance
    z11=((1+s11 ( i ) ) *(1-s22 ( i ) )+s12 ( i ) * s21 ( i
) ) /((1-s11 ( i ) ) *(1-s22 ( i ) )-...
        s12 ( i ) * s21 ( i ) ) ;
    z12=2*s12 ( i ) /((1-s11 ( i ) ) *(1-s22 ( i ) )-s12 (
i ) * s21 ( i ) ) ;
    z21=2*s21 ( i ) /((1-s11 ( i ) ) *(1-s22 ( i ) )-s12 (
i ) * s21 ( i ) ) ;
    z22=((1-s11 ( i ) ) *(1+ s22 ( i ) )+s12 ( i ) * s21 (
i ) ) /((1-s11 ( i ) ) *(1-s22 ( i ) )-...
        s12 ( i ) * s21 ( i ) ) ;
    %modified S parameter including source and load
impedance
    s21_n( i )=-50*z12 /( z12^2-(z11+50) * ( z22+50) ) ;
    i = i +1;
end
%Plot
figure(10);
f =30e6:5000:101e6 ;
y1 = 20*log10(abs( s21_n)) ;
y2 = angle(s21_n)*180/pi ;
yyaxis left
plot(f,y1,'r')
title( 'Frequency Response of delay line with N_{fp1}=6 and
N_{fp2}=3','FontSize',18);

```

```
xlabel ('Frequency (MHz)', 'FontSize', 18);  
ylabel ( 'dB' , 'FontSize' , 18)  
set(findall(gca, 'type', 'line'), 'linewidth', 1)  
yyaxis right  
plot (f, y2, 'g')  
ylabel ('Phase angle ( degrees )', 'FontSize' , 18)  
ylim([-200 200] )
```